Mush, Melts and Metasediments: a History of Rhyolites from the Okataina Volcanic Centre, New Zealand, as Captured in Plagioclase

May Sas [1]*, Phil Shane[1], Takeshi Kuritani[2], Georg F. Zellmer [3], Adam J. R. Kent[4] and Mitsuhiro Nakagawa[2]

[1]School of Environment, University of Auckland, Auckland 1142, New Zealand; [2]Natural History Sciences, Hokkaido University, Sapporo 060-0810, Japan; [3]Volcanic Risk Solutions, Massey University, Palmerston North 4442, New Zealand; [4]College of Earth, Ocean, and Atmospheric Sciences, Oregon State University, Corvallis, OR 97330, USA

*Corresponding author. Telephone: +1-360-650-7363. Fax: +1-360-650-7302. E-mail: sasm@wwu.edu

ABSTRACT

The Okataina Volcanic Centre (OVC), located in the Taupo Volcanic Zone, New Zealand, is a dominantly rhyolitic magmatic system in an arc setting, where eruptions are thought to be driven by mafic recharge. Here, Sr–Pb isotopes, and compositional and textural variations in plagioclase phenocrysts from 10 rhyolitic deposits (two caldera, one immediately post-caldera, four intra-caldera, and three extra-caldera) are used to investigate the OVC magmatic system and identify the sources and assimilants within this diverse mush zone. Plagioclase interiors exhibit normal and reverse zoning, and are commonly in disequilibrium with their accompanying glass, melt inclusions, and whole-rock compositions. This indicates that the crystals nucleated in melts that differed from their carrier magma. In contrast, the outermost rims of crystals exhibit normal zoning that is compositionally consistent with growth in cooling and fractionating melts just prior to eruption. At the intra-crystal scale, the total suite of $^{87}Sr/^{86}Sr$ ratios are highly variable ($0.7042–0.7065 \pm 0.0004$ average 2SE); however, the majority (95 %) of the crystals are internally homogeneous within error. At whole-crystal scale (where better precision is obtained), $^{87}Sr/^{86}Sr$ ratios are much more homogeneous ($0.70512–0.70543 \pm 0.00001$ average 2SE) and overlap with their host whole-rock Sr isotopic ratios. Whole-crystal Pb isotopic ratios also largely overlap with whole-rock Pb ratios. The plagioclase and whole-rock isotopic compositions indicate significant crustal assimilation (≥ 20 %) of Torlesse-like metasediments (local basement rock) by a depleted mid-ocean ridge mantle magma source, and Pb isotopes require variable fluid-dominant subduction flux. The new data support previous petrogenetic models for OVC magmas that require crystal growth in compositionally and thermally distinct magmas within a complex of disconnected melt-and-mush reservoirs. These reservoirs were rejuvenated by underplating basaltic magmas that serve as an eruption trigger. However, the outermost rims of the plagioclase imply that interaction between silicic melts and eruption-triggering mafic influx is largely limited to heat and volatile transfer, and results in rapid mobilization and syn-eruption mixing of rhyolitic melts. Finally, relatively uniform isotopic compositions of plagioclase indicate balanced contributions from the crust and mantle over the lifespan of the OVC magmatic system.

Key words: *rhyolite petrogenesis*; *Pb isotopes*; *Sr isotopes*; *magma*; *plagioclase*

INTRODUCTION

Caldera-forming centres are the source of the most catastrophic explosive eruptions on Earth (e.g. Self, 2006; Bachmann & Bergantz, 2008). Continuous efforts have been made to characterize compositional changes between eruptions that may illuminate any evolutionary trends among these voluminous magmatic systems. Studies examining isotopic fluctuations between pre-, during-, and post-caldera events have been especially helpful with identification of shifts in mantle versus crustal mass contributions to these systems. For example, volcanic systems associated with the Yellowstone hotspot (western USA) show periods with significant shifts in mantle contributions based on radiogenic isotope ratios ($\geq 25\%$ mass fluctuations during pre-8 Ma activity; Nash et al., 2006), as well as significant assimilation of crust and roof materials in post-caldera eruptions (e.g. Hildreth et al., 1984, 1991). At the Valles volcanic system (western USA), which is situated in a continental rift setting, silicic magmas are compositionally and isotopically distinct and require variable amounts of mantle-derived and lower crust components (e.g. Spell et al., 1993). This study examines whether similar isotopic shifts are present within a relatively young, frequently active, silicic magmatic system that is situated in a coupled subduction–extension setting of the Taupo Volcanic Zone (TVZ) in New Zealand.
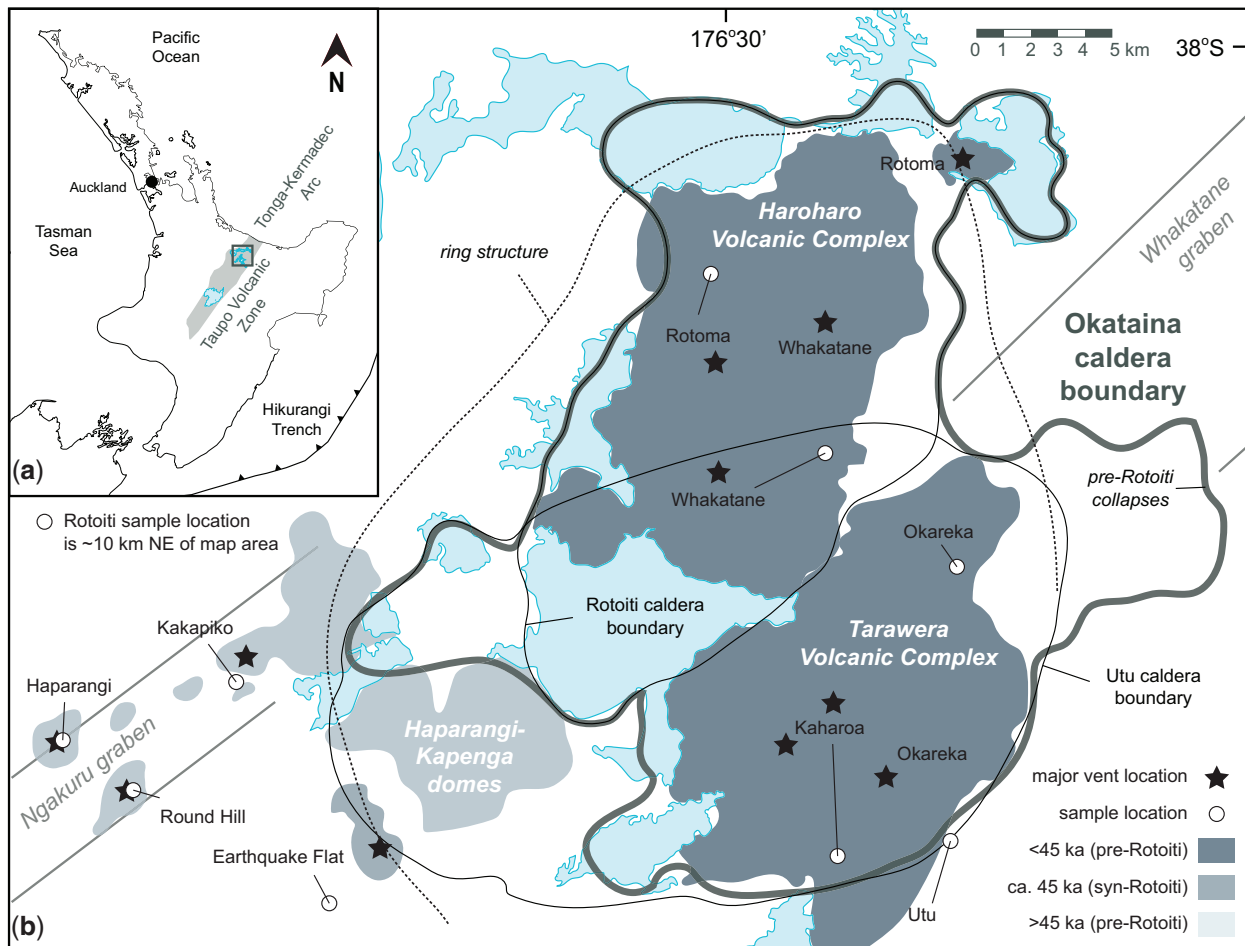
The Okataina Volcanic Centre (OVC) is located in the northeastern region of the central TVZ (Fig. 1) and experienced at least three caldera-forming events over the last 0·6 Myr (Nairn, 2002; Cole et al., 2014). There have been 11 intra-caldera eruptions since c. 22 ka, including a (basaltic) eruption in AD 1886 and the most recent rhyolitic eruption (AD 1314) in New Zealand (Nairn, 2002). The high frequency of volcanic activity has made the OVC a target for numerous petrological and eruption-sequence studies, which reveal an intricate magma storage system that has undergone magma mingling and thermal rejuvenation via basaltic underplating (e.g. Leonard et al., 2002; Nairn et al., 2004; Kobayashi et al., 2005; Shane et al., 2005a; Smith et al., 2005, 2006; Shane et al., 2008a). Additionally, zircon studies demonstrate that a long-lived (10^4–10^5 years) silicic reservoir exists beneath the OVC (Charlier et al., 2003; Charlier & Wilson, 2010; Klemetti et al., 2011; Storm et al., 2011, 2012, 2014; Rubin et al., 2017). Some eruptions have been fed by the contemporaneous tapping of magma reservoirs that occurred side-by-side on a kilometer-scale, but experienced separate thermal histories on a 100 000 year scale (Storm et al., 2011). Mingling of melts with differing thermal histories is also revealed in amphibole growth histories that require the disruption of a thermally zoned magmatic reservoir (Shane & Smith, 2013). Furthermore, plagioclase growth histories indicate increased mafic recharge of the system immediately following (within c. 5–10 kyr) caldera-forming events (Shane, 2015).

Despite the substantial framework that these studies provide, magma sources and their isotopic signatures have not been fully explored. It is not known whether magmas formed from isotopically heterogeneous sources, and whether such relic signatures are identifiable. Moreover, the importance of basaltic magmas in rejuvenating the OVC rhyolite system is clearly indicated by the presence of basaltic components on a microscopic scale in some deposits (e.g. Hiess et al., 2007; Shane et al., 2008a; Barker et al., 2020). However, the mass (i.e. liquid, volatiles) and thermal budget of the basaltic mixing events, and the degree of mixing between the resident rhyolitic body and the mafic intrusions, is uncertain. Investigations of mineral isotopic compositions at other volcanoes, albeit mostly intermediate arc magmas, have elucidated such processes and have been crucial to refining our understanding of magmatic origins, with plagioclase proving to be particularly useful for insights (e.g. La Garita, Charlier et al., 2007; Merapi, Chadwick et al., 2007; Chaos Crags, Tepley et al., 1999; Parinacota, Ginibre & Davidson, 2014). However, although some work has been done (Charlier et al., 2007, 2008; Wolff & Ramos, 2014), less is known about the isotopic heterogeneity of plagioclase in high-SiO_2 rhyolite magmas erupted at calderas. Plagioclase is highly responsive to shifts in crystallization conditions, which makes it ideal for distinguishing between processes such as volatile, pressure, and melt composition fluctuations (e.g. Singer et al., 1995; Ginibre et al., 2002, 2007; Ruprecht & Wörner, 2007; Shane, 2015). Because plagioclase readily incorporates Sr into its structure (Sr^{2+} replaces Ca^{2+} in the plagioclase crystal lattice; Blundy & Wood, 1991), relatively high Sr concentrations allow for reliable $^{87}Sr/^{86}Sr$ investigations on an intra-crystal scale (e.g. Tepley et al., 2000; Davidson et al., 2007; Ramos & Tepley, 2008). Strontium isotopic analyses can be further coupled with Pb isotopic compositions to better characterize sources (e.g. McCulloch et al., 1994). Thus, we set out to identify fluctuations and patterns in isotopic sources on a crystal, eruption, and volcano scale by examining trace element variations, mineral textures, and Sr and Pb isotopic compositions in plagioclase, a ubiquitous mineral phase in OVC deposits. We have evidence for a surprisingly balanced interaction between the mantle and the crust over the lifespan of the magmatic system.

GEOLOGICAL SETTING AND BACKGROUND

The OVC is located in the northeastern region of the central TVZ, which extends about 200 km across central North Island and is the southwestern subaerial terminus of the submarine Tonga–Kermadec volcanic arc (Fig. 1) (Wilson et al., 1995). Current subduction rates at the concomitant Hikurangi Trench vary dramatically from north (58 mm a^{-1}) to the south (19 mm a^{-1}), where the margin between the Pacific and Australian plates changes from convergent to transform (Wallace et al., 2009). Volcanism across the TVZ is also influenced by extension (12 mm a^{-1} at the OVC) and trench-ward rotation of the eastern North Island region (Wallace et al., 2004). In addition to developing ample dike

Fig. 1. Map of the Okataina Volcanic Centre (OVC) in the Taupo Volcanic Zone (TVZ, inset map) of North Island, New Zealand. Okataina caldera boundaries (continuous outlines), ring structure (dotted outline), dome complexes (dark gray regions), and grabens (gray lines) are from Nairn (2002). Stars represents the dominant vent location(s) for each dome eruption, and are amalgamated from Nairn (2002), Nairn *et al.* (2004), Smith *et al.* (2006), and Shane *et al.* (2008a).

and sill structures that allow and control magma migration and storage (Spinks *et al.*, 2005; Shane *et al.*, 2008b; Cole *et al.*, 2010), rifting across the TVZ also leads to crustal thinning, elevated rates of magma emplacement, and further decompression of the underlying mantle (Stern & Benson, 2011; Cole *et al.*, 2014). The crust–mantle boundary lies *c.* 25 km below the TVZ, and the mid- to lower crust is heavily intruded and/or consists of magmatic bodies with large amounts of partial melts (Bannister *et al.*, 2004; Harrison & White, 2006; Heise *et al.*, 2010).

Silicic TVZ magmas are understood to be secondary products, which form via fractional crystallization of mantle partial melts that are significantly modified by crustal contamination. This is evident from whole-rock Sr–Nd–Pb ratios of all TVZ mafic to silicic magmas, which fall on a mixing trend between regional Mesozoic Torlesse metasedimentary crustal rocks and Tonga–Kermadec arc basalts (Gamble *et al.*, 1993, 1994, 1996; Graham *et al.*, 1995; Price *et al.*, 2012, 2015). This is also supported by the presence of Mesozoic–Paleozoic

xenocrystic zircons (Charlier *et al.*, 2005) in TVZ deposits. Crustal assimilation, based on radiogenic and stable isotope models, has been estimated to range from 10 % for basalts and andesites to as much as 25 % for rhyolites (Graham *et al.*, 1992, 1995; McCulloch *et al.*, 1994). Importantly, work on southern TVZ andesites requires a more complicated petrogenetic model that also involves a lower crustal oceanic meta-igneous component(s) as the source for some parental magmas, and this may also apply elsewhere in the TVZ (Price *et al.*, 2012).

Two dominantly rhyolitic volcanic centers in the TVZ are considered dormant, namely the OVC and the Taupo Volcanic Centre, and of the two the OVC is the oldest (*c.* 0·6 Ma) and latest to erupt (Houghton *et al.*, 1995; Nairn, 2002; Cole *et al.*, 2010, 2014). Volcanism since the youngest caldera-forming eruption (45 ka; Danišík *et al.*, 2012) occurred across two parallel vent complexes within the limits of the OVC caldera boundary, which are potentially continuations of the regional grabens (Fig. 1) (Nairn, 2002). The Tarawera Volcanic

Complex erupted most recently and is located in the southern region of OVC, and the Haroharo Volcanic Complex encompasses the northern region (Fig. 1) (Nairn, 2002). Although deposits at the OVC are both silicic and mafic in composition, most volcanic products are rhyolitic and intermediate compositions are rare. Deposits studied here are all high-SiO_2 rhyolites and consist of the oldest and youngest caldera-forming eruptions, an immediately post-caldera eruption, two Tarawera Volcanic Complex eruptions, two Haroharo Volcanic Complex eruptions, and three extra-caldera dome eruptions (pre-youngest caldera-forming eruption). Deposit properties are summarized in Table 1 and sample localities are shown in Fig. 1.

METHODS

Sample preparation and major and minor element analyses of plagioclase from all units, as well as Fe–Ti oxides, glass, and whole-rocks from the extra-caldera domes (to fill in gaps in the literature), are detailed in the Supplementary Data; supplementary data are available for downloading at http://www.petrology.oxfordjournals.org. Trace element and Sr–Pb isotopic analyses of plagioclase from all units, as well as whole-rock Pb isotopic analyses of all samples and Sr isotopic analyses of extra-caldera domes, Whakatane, Rotoma, and Rotoiti, are detailed below. All data, including standard analytical information, are provided in Supplementary Data Tables A1–A6.

Plagioclase geochemistry and isotopes

Trace element contents of plagioclase were measured at the University of Auckland by laser ablation inductively coupled plasma mass spectrometry (LA-ICP-MS) using an Agilent 7700 Series ICP-MS system with s-lens, equipped with an Australian Scientific Instruments RESOlution 193 nm excimer LA system. Analytical settings consisted of 80 μm ablation spots, 2·5 J cm^{-2} fluence, and 5 Hz s^{-1} pulse rate. The total run time per spot was 65 s, with a delay of 60 s between analyses. Ablated material was carried to the plasma torch using He at a flow rate of 0·4 l min^{-1}. Masses analyzed were ^{7}Li, ^{25}Mg, ^{29}Si, ^{43}Ca, ^{47}Ti, ^{55}Mn, ^{66}Zn, ^{71}Ga, ^{85}Rb, ^{88}Sr, ^{89}Y, ^{90}Zr, ^{93}Nb, ^{133}Cs, ^{138}Ba, ^{139}La, ^{140}Ce, ^{141}Pr, ^{146}Nd, ^{147}Sm, ^{153}Eu, ^{157}Gd, ^{159}Tb, ^{163}Dy, ^{165}Ho, ^{166}Er, ^{169}Tm, ^{172}Yb, ^{175}Lu, ^{208}Pb, ^{232}Th, and ^{238}U, with precision of 1–8% (2SD) for elements reported in this study. To check for fractionation, the ^{232}Th/^{238}U ratio of the standard was monitored throughout analyses. Oxide ratios were monitored using ^{248}ThO/^{232}Th ($<$0·45%). LA-ICP-MS spots were placed in the same compositional zones as analyzed using the microprobe, and CaO contents were used as an internal standard to calibrate the LA-ICP-MS data. NIST610 was used for instrument tuning, BHVO-2 glass ($n = 19$) was used as the standard throughout the analytical session, and BCR-2 glass ($n = 20$) was a secondary standard run as an unknown (Raczek *et al.*,

2001). Plagioclase LA-ICP-MS analyses and standards are reported in Supplementary Data Table A2.

Intra-crystal Sr isotopic ratios of plagioclase were measured using a Photon Machines G2 193 nm excimer laser ablation system connected to a Nu Plasma multi-collector (MC-)ICP-MS system at the Oregon State University W. M. Keck Collaboratory for Plasma Mass Spectrometry. Ablation used a 100 μm diameter spot, and the sample was translated at 5 μm s^{-1} to produce troughs that varied in length from 300 to 600 μm depending on the crystal size (longer troughs, $\geq$450 μm, were analyzed where possible). Helium was used as the carrier gas to transport the sample material from the ablation chamber to the plasma torch with a flow rate of 0·3 l min^{-1}. Fluence was set at 4·84 J cm^{-2} throughout analyses, and laser pulse rates were 15 Hz s^{-1} for standards and 30 Hz s^{-1} for plagioclase. A total of six masses, 83, 84, 85, 86, 87, and 88, were measured. Mass bias corrections, as well as ^{87}Rb contributions (calculated from measured ^{85}Rb), were applied using a measured ratio of ^{86}Sr/^{88}Sr = 0·1194. To correct for gas species (e.g. Kr) introduced by the plasma, on-peak corrections were made by subtracting measured background values from measured intensities. Calcium species were not monitored, as contributions from Ca dimers and argides were deemed trivial by previous studies (Miller & Kent, 2009). Instrument tuning was completed using NIST610 glass, and an internal standard used throughout analyses was a modern gastropod with ^{87}Sr/^{86}Sr = 0·709190 $\pm$ 0·000008 (Miller & Kent, 2009). The average measured gastropod ratio throughout analyses was ^{87}Sr/^{86}Sr = 0·70942 $\pm$ 0·00017 (2SD, $n = 134$) (Supplementary Data Table A2). Any offset between the measured and accepted gastropod ratio was corrected for during data reduction. Plagioclase errors were also propagated together with gastropod errors to correct for any machine fractionation, which, along with lower Sr concentrations in the unknowns relative to the standard, resulted in higher internal reproducibility relative to external reproducibility (Supplementary Data Fig. A1). To monitor instrument accuracy, a high-Sr, low-Rb clinopyroxene was used as a secondary standard (^{87}Sr/^{86}Sr = 0·704470 $\pm$ 0·000017 and 0·704482 $\pm$ 0·000010; Burns *et al.*, 2015) and analyzed as an unknown, with average ^{87}Sr/^{86}Sr = 0·70446 $\pm$ 0·00018 (2SD, $n = 68$) across all analyses. Additional Kaharoa and Rotoma plagioclase compositions and LA-MC-ICP-MS ^{87}Sr/^{86}Sr data analyzed using a similar set-up, but smaller spot diameter (65–80 μm), have been included from Sas *et al.* (2019). Between 17 and nine crystals have been analyzed per unit ($n = 10$ for most). LA-MC-ICP-MS Sr isotopic ratios are summarized in Supplementary Data Table A2.

Additional isotopic analyses were performed on single- or multi-crystal (1–4 mg) scale (herein whole-crystal) to obtain Pb isotopic compositions of plagioclase (one to three analyses per unit). Whole-crystal Sr isotopic analyses were completed on the same crystals. Only plagioclase crystals that appeared inclusion-free were carefully selected using an optical microscope. Sample preparation and processing for Pb column

Table 1 Summary table of studied unit

Eruption	Eruption type	Age (ka)	Volume (km³)	Unit[1]	Mineralogy[2]	P (kbar)[3]	T(°C)[4]	fO_2 (NNO)	References
Kaharoa (KA)	Domes (Tarawera)	0.7	9.1	T2	plg > qtz ≫ bio > Fe–Ti ± hbl, opx, cgt (5–40 %)	1.6	724 ± 16	+0.00 ± 0.54	Shane (1998); Leonard et al. (2002); Hogg et al. (2003); Nairn et al. (2004)†*; Smith et al. (2005); Sahetapy-Engel et al. (2014)
Whakatane (WT)	Domes (Haroharo)	5.5	11.3	WT1	qtz > plag ≫ hbl > cgt > Fe–Ti > opx (10–20 %)	1.2	745 ± 11	+0.34 ± 0.08	Nairn (2002); Kobayashi et al. (2005); Smith et al. (2006)†*; Lowe et al. (2008)
Rotoma (RM)	Domes (Haroharo)	9.5	8	RT2	plg > qtz ≫ Fe–Ti > opx > cgt (10–20 %)	1.2	760 ± 9	+0.62 ± 0.06	Smith et al. (2005, 2006)†*; Lowe et al. (2008)
Okareka (OK)	Domes (Tarawera)	21.8	5	T3	plg > qtz ≫ opx + hbl + cgt + Fe–Ti ≫ bio (9–34 %)	1.2	794 ± 12	+0.82 ± 0.08	Nairn (2002); Smith et al. (2005); Lowe et al. (2008); Shane et al. (2008a)†*
Earthquake Flat (EQ)	Post-caldera	c. 45	10	—	plg > qtz ≫ bio > hbl > Fe–Ti ± opx (25–45 %)	2	754 ± 52	−0.26 to +0.32	Davis (1985); Froggatt & Lowe (1990); Smith et al. (2005, 2010); Molloy et al. (2008)*
Rotoiti (RT)	Caldera	45	120	T1	plg > qtz ≫ cgt > Fe–Ti > hbl > opx (15–25 %)	2	766 ± 13	+0.92 ± 0.09	Schmitz & Smith (2004); Shane et al. (2005)†*; Smith et al. (2005); Danišik et al., (2012)
Kakapiko (KP)	Dome	200–45	—	hk_2	qtz > plg ≫ bio > hbl > opx + Fe–Ti (20–40 %)	—	722 ± 13	−0.19 ± 0.10	Nairn (2002)†, this study
Haparangi (HA)	Dome	200	—	hk_2	qtz > plg ≫ bio ≫ hbl > opx + Fe–Ti (20–40 %)	—	718 ± 15	−0.47 ± 0.12	Nairn (2002)†, this study
Round Hill (RH)	Dome	325–45	—	hk_2	qtz > plg ≫ bio > hbl > opx + Fe–Ti (20–40 %)	—	724 ± 13	−0.28 ± 0.11	Nairn (2002)†, this study
Utu (UT)	Caldera	557	90	—	qtz/plg > bio ≫ hbl > opx + Fe–Ti (15–25 %)	—	762 ± 8	−0.52 ± 0.10	Nairn (2002); Deering et al. (2008, 2010)*; Cole et al. (2010, 2014); Leonard et al. (2010)

[1]Unit represents the eruption unit extracted plagioclase from, as named and described in the respective reference (marked with †). Units selected are the most voluminous or hybridized units.
[2]Mineral abbreviations: plg, plagioclase; qtz, quartz; bio, biotite; hbl, hornblende; cgt, cummingtonite; opx, orthopyroxene; Fe–Ti, Fe–Ti oxides. Percentages represent the range of crystal abundances throughout each eruption. Source for mineralogy and percentages marked with *.
[3]Pressure listed is minimal pressure in literature.
[4]Representative temperatures calculated from Fe–Ti oxide pairs using the method of Ghiorso & Sack (1991), from literature and this study.

Table 2 Average whole-rock, glass, and melt inclusion analyses for OVC units

Eruption:	Kaharoa			Whakatane			Rotoma			Okareka			Earthquake Flat				Rotoiti				Kakapiko		Haparangi		Round Hill		Utu	
Analysis:[1]	wr	g	mi_Q	wr	g	mi_Q	wr	g	mi_Q	wr	g	mi_Q	wr	g	mi_Q	mi_P	wr	g	mi_Q	mi_P	wr	g	wr	g	wr	g	wr	g
SiO_2	76.44	77.51	77.19	76.60	77.76	77.71	76.38	77.70	77.56	75.98	77.75	77.66	72.24	77.06	74.06	73.46	73.66	73.90	74.06	73.30	73.94	77.52	73.68	77.35	74.15	77.57	74.11	77.57
TiO_2	0.16	0.11	0.42	0.20	0.17	0.12	0.21	0.17	0.12	0.22	0.18	0.09	0.29	0.14	0.10	0.10	0.27	1.67	0.10	0.13	0.27	0.12	0.27	0.12	0.28	0.12	0.25	0.14
Al_2O_3	12.69	12.46	12.52	12.81	12.21	12.58	13.06	12.29	12.66	13.16	12.29	12.51	14.22	12.19	11.82	11.91	13.79	10.38	11.82	11.88	13.87	12.03	14.22	12.07	13.78	12.07	14.57	12.16
Fe_2O_3	1.26	—	—	1.48	—	—	0.63	—	—	1.62	—	—	2.16	—	—	—	1.98	—	—	—	2.13	—	2.21	—	2.17	—	1.94	—
FeO	0.78	0.79	0.84	0.26	0.84	0.88	1.09	0.89	0.91	0.70	0.94	0.86	1.62	0.89	0.98	0.94	1.34	0.90	0.98	1.00	—	0.92	—	0.95	—	0.95	—	0.84
MnO	0.06	0.07	0.05	0.06	0.08	0.05	0.06	0.08	0.06	0.06	0.08	0.05	0.06	0.07	0.05	0.06	0.08	0.05	0.05	0.04	0.07	0.10	0.07	0.11	0.07	0.11	0.05	0.07
MgO	0.23	0.05	0.08	0.24	0.10	0.11	0.25	0.13	0.13	0.26	0.13	0.07	0.46	0.09	0.07	0.09	0.45	0.13	0.07	0.15	0.41	0.09	0.40	0.04	0.42	0.04	0.39	0.09
CaO	1.07	0.51	0.66	1.25	0.74	0.74	1.33	0.83	0.83	1.35	0.86	0.69	2.02	0.79	0.70	0.73	1.89	0.82	0.70	0.85	1.80	0.64	1.69	0.63	1.78	0.63	1.67	0.74
Na_2O	4.15	4.10	3.84	4.18	4.19	3.85	4.21	4.30	3.96	4.02	3.88	3.74	3.78	3.70	3.05	3.17	3.89	3.62	3.05	3.00	4.16	3.91	4.24	3.91	4.09	3.84	3.70	3.83
K_2O	3.41	4.23	4.20	3.15	3.74	3.75	2.99	3.46	3.57	3.26	3.74	4.12	2.75	4.50	4.41	4.23	2.47	3.24	4.41	3.38	3.15	4.39	3.02	3.91	3.10	3.84	3.32	4.34
P_2O_5	0.04	—	—	0.03	—	—	0.03	—	—	0.03	—	—	0.05	0.01	0.02	0.00	0.04	0.02	0.02	0.03	0.05	0.64	0.04	0.04	0.04	3.10	0.01	0.01
n	27	58	165	23	16	52	25	21	29	21	59	94	60	239	11	4	79	162	114	11	7	10	5	10	2	10	15	10
H_2O	—	3.11	5.18	—	2.67	4.48	—	2.97	5.26	—	4.58	5.12	—	4.24	4.99	5.04	—	3.42	4.99	5.37	—	3.97	—	3.97	—	5.07	—	3.87
H_2O SD	—	1.97	0.68	—	1.21	0.66	—	1.19	0.30	—	2.17	1.45	—	0.97	1.37	1.28	—	1.78	1.37	1.05	—	1.65	—	1.65	—	1.99	—	1.01
H_2O n	—	27	28	—	16	14	—	21	2	—	12	16	—	205	35	4	—	29	35	4	—	10	—	10	—	10	—	10
Mg	1358	276	509	1420	589	683	1499	784	776	1555	783	444	2750	534	448	548	2718	786	448	930	2498	547	2436	547	2533	240	2379	548
Sr	83	27	47	105	41	63	118	58	71	107	56	47	158	42	35	38	152	51	66	63	148	—	137	—	147	—	138	—
Ba	908	806	879	830	819	900	797	861	860	810	771	754	663	771	711	680	803	871	850	734	759	—	738	—	744	—	764	—
La	26	18	23	24	21	24	23	22	23	27	21	24	26	22	20	19	—	20	20	17	25	—	26	—	26	—	22	—
Ce	53	41	49	46	47	51	46	48	51	54	41	49	41	42	38	37	20	39	40	33	50	—	49	—	49	—	51	—

[1] wr, whole-rock; g, glass; mi_Q, quartz melt inclusions; mi_P, plagioclase melt inclusions. Oxides are in wt%; elements are in ppm.

[2] Data extracted from studies include representative compositions (if individual analyses are not provided), thus n is greater than listed above for ≤45 ka units.

Sources are as follows. Kaharoa: Leonard et al. (2002); Nairn (2002); Nairn et al. (2004); Smith et al. (2005); Shane & Smith (2013). Whakatane: Nairn (2002); Smith et al. (2005, 2006); Johnson et al. (2013); Shane & Smith (2013). Rotoma: Nairn (2002); Smith et al. (2005, 2006); Shane & Smith (2013). Okareka: Nairn (2002); Smith et al. (2005); Shane et al. (2008a, 2008b); Molloy et al. (2009); Johnson et al. (2013). Earthquake Flat: Nairn (2002); Schmitz & Smith (2004); Smith et al. (2005, 2010); Molloy et al. (2008); Shane & Smith (2013). Rotoiti: Nairn (2002); Schmitz & Smith (2004); Shane et al. (2005a); Smith et al. (2005, 2010); Molloy et al. (2008); Johnson et al. (2013); Shane & Smith (2013). Kakapiko, Haparangi, and Round Hill, present study. Utu: Nairn, (2002); Deering et al. (2008); Cole et al. (2010). Nairn (2002) data include references therein. Sample 559-1 from Smith et al. (2010) and Shane et al. (2005a) was omitted owing to described devitrification, and mi_Q inclusion 807 from Shane et al. (2008b) was omitted owing to abnormal values.

chromatography followed the methods of Kuritani & Nakamura (2002). The residuals were processed using Sr column chromatography following the methods of Pin et al. (1994). Strontium isotopic ratios were determined using a solution MC-ICP–MS system (NeptunePlus, Thermo Fisher Scientific) located at the Graduate School of Science at Hokkaido University. Mass fractionation factors were internally corrected using $^{86}Sr/^{88}Sr = 0.1194$. The average mass fractionation-corrected isotopic ratio of NIST987 was $^{87}Sr/^{86}Sr = 0.710283 \pm 0.000026$ (2SD, $n = 5$). Corrections were performed on the $^{87}Sr/^{86}Sr$ ratios of the samples by applying a standard bracketing method using NIST987 and normalizing to $^{87}Sr/^{86}Sr = 0.710240$ (Makishima & Masuda, 1994). A secondary standard, the Geological Survey of Japan (GSJ) basaltic reference material JB-3 (Imai et al., 1995) ($^{87}Sr/^{86}Sr = 0.703410 \pm 0.000005$ 2SD; Miyazaki & Shuto, 1998), was analyzed as an unknown. The average Sr isotopic ratio of JB-3 was $^{87}Sr/^{86}Sr = 0.703411 \pm 0.000009$ (2SD, $n = 3$). Lead isotopic ratios were determined using the same MC-ICP-MS system with a CETAC Aridus II^{TM} desolvating nebulizer system. Mass fractionation factors were internally corrected using Tl ($^{205}Tl/^{203}Tl = 2.3871$; Dunstan et al., 1980). Two standards were analyzed and used for sample corrections, JB-3 ($^{206}Pb/^{204}Pb = 18.2954 \pm 0.0042$, $^{207}Pb/^{204}Pb = 15.5380 \pm 0.0044$, and $^{208}Pb/^{204}Pb = 38.2516 \pm 0.0111$, 2SD; Kuritani et al., 2006) and an in-house basaltic standard HK1103 ($^{206}Pb/^{204}Pb = 18.8156 \pm 0.00007$, $^{207}Pb/^{204}Pb = 15.6268 \pm 0.0008$, and $^{208}Pb/^{204}Pb = 38.9431 \pm 0.0026$, 2SD, $n = 3$; this study). A third standard, the GSJ rhyolitic reference material JR-1 (Imai et al., 1995) ($^{206}Pb/^{204}Pb = 18.3616 \pm 0.008$, $^{207}Pb/^{204}Pb = 15.5650 \pm 0.0007$, and $^{208}Pb/^{204}Pb = 38.4190 \pm 0.0023$, 2SD, $n = 6$; this study), was analyzed as an unknown. Measured Pb isotopic ratios for JR-1 ($\sim$10 ng Pb) during the course of this study were $^{206}Pb/^{204}Pb = 18.3636 \pm 0.0017$, $^{207}Pb/^{204}Pb = 15.5645 \pm 0.0021$, and $^{208}Pb/^{204}Pb = 38.4213 \pm 0.0090$ (2SD, $n = 5$). The isotopic ratios of the two standard samples, HK1103 and JR-1, were accurately determined for large sample sizes ($\sim$500 ng) using the MC-ICP-MS system without the use of the desolvating nebulizer system (described below with whole-rock isotopes). The total procedural blanks for Sr and Pb are approximately 100 pg and 30 pg, respectively, and are negligible compared with the amounts of the Sr and Pb in the samples (300–2500 ng and 2–25 ng, respectively). Plagioclase Sr and Pb isotopic ratios obtained via solution ICP-MS are summarized in Supplementary Data Table A3.

Whole-rock isotopes
Sr isotopes
All whole-rock Sr isotopic compositions that are available in the literature and used in this study are listed in Supplementary Data Table A6. Additional Sr isotopes for Whakatane ($n = 2$), Rotoma ($n = 2$), Rotoiti ($n = 3$), and the three extra-caldera domes ($n = 1$ per unit) were measured by MC-ICP-MS at the Victoria University of Wellington Geochemistry Laboratory. All samples were leached in 6M HCl for 5 min at room temperature, then agitated using an ultrasonicator, centrifuged and rinsed three times using milli-Q water. This full leaching and rinsing cycle was repeated 2–3 times per sample. Samples were dissolved using 3 parts concentrated HF and 1 part concentrated HNO_3 and Sr separation was completed using a double pass through Eichrom chromatographic Sr Specific resin by elution of the sample matrix in 3M HNO_3 and Sr collection in milli-Q water. Correction for instrumental mass bias was done by normalization to $^{86}Sr/^{88}Sr = 0.1194$, with all data reported to $^{87}Sr/^{86}Sr = 0.710240$ for NIST987 (Makishima & Masuda, 1994). A basaltic standard (BHVO-2, $^{87}Sr/^{86}Sr = 0.703435 \pm 0.000010$; Raczek et al., 2003) was analyzed among unknowns and yielded $^{87}Sr/^{86}Sr = 0.703468 \pm 0.000006$ (2SD, $n = 5$). Whole-rock isotopic compositions and standards are reported in Supplementary Data Table A6.

Pb isotopes
Whole-rock Pb isotopic compositions were determined for all units, as well as HK1103 and JR-1, by MC-ICP-MS at the Graduate School of Science at Hokkaido University, without the use of a desolvating nebulizer. Sample preparation procedures were the same as described above for plagioclase. Mass fractionation for Pb was internally corrected using Tl. The average mass fractionation-corrected isotopic ratios of NIST981 during analyses were typically $^{206}Pb/^{204}Pb = 16.9340$, $^{207}Pb/^{204}Pb = 15.4881$, and $^{208}Pb/^{204}Pb = 36.6877$. Corrections were performed on the Pb ratios of the samples by applying a standard bracketing method using NIST981 and normalizing to the reported NIST981 ratios of $^{206}Pb/^{204}Pb = 16.9424$, $^{207}Pb/^{204}Pb = 15.5003$, and $^{208}Pb/^{204}Pb = 36.7266$ (Kuritani & Nakamura, 2003). Whole-rock Pb isotopic ratios obtained via solution ICP-MS are summarized in Supplementary Data Table A6.

RESULTS
Plagioclase textures and compositions
Plagioclase crystals throughout the units are euhedral tabular laths commonly 1–2 mm in length, although larger crystals ($\leq$4 mm) are noted in $\geq$45 ka units. Plagioclase cores are commonly resorbed, whereas plagioclase rims generally exhibit equilibrium textures. Although plagioclase crystals display a diverse array of textures and anorthite (An) contents, with An = [100*Ca/(Ca + Na + K)], they share commonalities that allow them to be categorized into four textural groups. Two groups exhibit normal zoning (An decrease from interior to rim, groups 1 and 2), and two groups exhibit reverse zoning (An increase from interior to rim along with a dissolution boundary, groups 3 and 4). However, even in the reversely zoned crystals, the outermost crystal rims display normal zoning. Textural groups are summarized in Fig. 2 and representative crystals are shown in Fig. 3. Overall, the range in An contents within plagioclase rims (An_{48-22}) is less than within plagioclase cores (An_{77-19}).

Table 3 Compositions used for mixing models

	Possible parental melts		OVC basalt	Possible assimilant		Possible crustal contaminants	
Description:	Primitive basalt	Subduction-modified basalt	OVC basalt	Torlesse (metasediments)	Metasedimentary xenolith	Waipapa (metasediments)	Metaigneous xenoliths
Location:	Ngatoro Basin	Rumble IV	Tarawera	E of TZV	S TVZ	W of TZV	S TVZ
Sample name:	VUW158/4[1]	VUW162/1[1]	Tarawera[2]	rep[3]	R97/104A[4]	rep[3]	rep[5]
SiO_2	50·74	50·88	50·95	70·31	47·84	63·01	52·33
TiO_2	1·45	0·87	0·83	0·51	1·19	0·86	1·03
Al_2O_3	16·15	18·30	17·18	15·41	25·82	16·69	16·92
Fe_2O_3	1·14	1·15	10·26	3·97	4·17	6·37	13·45
FeO	7·59	7·68			3·68		
MnO	0·16	0·17	0·17	0·06	0·08	0·12	0·17
MgO	7·03	5·08	6·20	1·31	3·27	2·12	7·95
CaO	9·42	11·12	11·43	1·57	8·21	2·25	8·85
Na_2O	3·75	2·62	2·34	3·78	3·66	3·97	2·03
K_2O	0·42	0·45	0·56	2·96	0·41	2·50	0·35
P_2O_5	0·15	0·11	0·13	0·12	0·22	0·20	0·13
Sc	30	30	41	11	18·6	16	33
V	255	300	255	64	162	125	248
Cr	300	64	45	28	78	28	362
Ni	104	32	12	9	21	12	125
Cu	48	90	24	2	28	18	57
Zn	80	76	88	64	143	81	115
Ga	19	19	17	23	40	18	20
Rb	6	8	16	118	11	78	13
Sr	172	288	309	295	517	379	378
Y	31	20	18	26	19	22	19
Zr	107	57	72	199	266	189	84
Nb	2	2	3	14	17	8	10
Ba	66	187	204	589	394	641	173
La	5	5	7	41	41	21	8
Ce	17	16	16	78	76	46	19
Nd	11	10	11	35	33	22	8
Sm			3	7	6	4	2
Eu			1	1	2	1	1
Gd			3	5	5	4	4
Tb			0·5	1	0·6	1	1
Dy			3	5	3	4	4
Ho			0·7	1·1	0·6	0·7	0·9
Er			2	3	2	2	2
Yb			2	3	2	2	3
Lu			0·3	0·7	0·3	0·3	0·4
Pb	6	7	5	27	6	17	7
Th	2	1	2	9	8	9	1
U			0·4	4	3	2	0·5
$^{87}Sr/^{86}Sr$	0·70295	0·70400	0·70523	0·70955	0·70724	0·70589	0·70665
$^{143}Nd/^{144}Nd$	0·513061	0·512977	0·512738	0·512432	0·512409	0·512665	0·512920
$^{206}Pb/^{204}Pb$	18·611	18·759	18·763	18·900	19·100	18·782	18·786
$^{207}Pb/^{204}Pb$	15·545	15·589	15·581	15·645	15·840	15·62	15·612
$^{208}Pb/^{204}Pb$	38·296	38·583	38·544	38·782	39·340	38·661	38·644

[1]Composition from Gamble *et al.* (1994), Sr–Nd–Pb isotopic ratios corrected from Gamble *et al.* (1996).
[2]Composition averaged from Gamble *et al.* (1993), Leonard *et al.* (2002), Nairn, (2002), Nairn *et al.* (2004), Hiess *et al.* (2007) and Zellmer *et al.* (2020), Sr–Nd isotopic ratios corrected from Gamble *et al.* (1996), Pb isotopic ratios uncorrected from Graham *et al.* (1992).
[3]Compositions and corrected Sr–Nd–Pb isotopic ratios from Price *et al.* (2015) (ss:mst 2:1 representative compositions).
[4]Compositions and corrected Sr–Nd–Pb isotopic ratios from xenolith (in Ruapehu andesite) of Price *et al.* (2012, 2015).
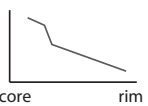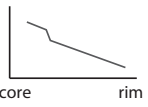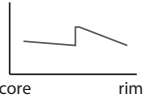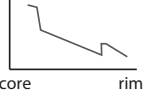[5]Average MIX composition and uncorrected Pb isotopic ratios from Price *et al.* (2012), average Sr–Nd isotopic ratios averaged and corrected from Graham *et al.* (1990), Price *et al.* (2012) and Waight *et al.* (2017).

Textural group 1 (T1) crystals have higher-An cores (An$_{71–33}$) with lower-An rims (An$_{38–22}$), a typically sharp boundary between the core and rim, and represent approximately 35 % of the plagioclase crystal population (Fig. 3a and l). T1 crystals are found in all 10 units. Textural group 2 (T2) crystals have resorbed, higher-An cores (An$_{59–31}$) with lower-An rims (An$_{40–21}$) and compose approximately 35 % of the crystal population (Fig. 3e–j). T2 crystals are found in all units except Rotoma.

Textural group 3 (T3) crystals have lower-An cores (An$_{39–19}$) with higher-An rims (An$_{48–24}$), and the boundary between cores and rims is resorbed, although the degree of dissolution varies from subtle to pronounced (Fig. 3d and k). T3 crystals compose approximately 25 % of the crystal population and are found in all units.

Textural group 4 (T4) crystals have resorbed, higher-An (An$_{77–51}$) cores with lower-An mantles and rims (An$_{39–25}$). The boundary between mantles and rims is

Group	An profiles	Texture	Description	An	$^{87}Sr/^{86}Sr$	Units
T1	core — rim		Normally-zoned with higher-An cores and lower-An rims ~35% of crystal population	Cores: 71-33 Rims: 38-22	Cores: 0.7043 - 0.7061 Rims: 0.7042 - 0.7061	All
T2	core — rim		Resorbed, higher-An cores with lower-An, normally-zoned rims ~35% of crystal population	Cores: 59-31 Rims: 40-21	Cores: 0.7045 - 0.7064 Rims: 0.7043 - 0.7061	All except Rotoma
T3	core — rim		Lower-An cores with higher-An rims and resorption along the core-rim boundary Outmost rims are normally-zoned ~25% of crystal population	Cores: 39-19 Rims: 48-24	Cores: 0.7046 - 0.7060 Rims: 0.7042 - 0.7065	All
T4	core — rim		Resorbed, higher-An cores with lower-An middles and rims and resorption along the middle-rim boundary Outmost rims are normally-zoned ~5% of crystal population	Cores: 77-51 Rims: 39-25	Cores: 0.7053 - 0.7057 Rims: 0.7049 - 0.7059	Kaharoa, Rotoma, Okareka, Rotoiti

Fig. 2. Illustrations and descriptions of characteristic plagioclase textural groups observed in OVC rhyolitic units. Brighter regions in the illustrations represent higher An contents and wavy boundaries represent dissolution.

resorbed, and the rim compositional zone along the dissolution boundary is always higher-An relative to the preceding mantle compositional zone (Fig. 3b and c). T4 crystals compose about 5% of the crystal population and are found only in the ≤45 ka units of Kaharoa, Rotoma, Okareka, and Rotoiti.

To reiterate, the outermost rims of all plagioclase crystals are normally zoned.

Major and trace element compositions
Major and trace element analyses of plagioclase are reported in Supplementary Data Tables A1 and A2, respectively. Major element analyses of Fe–Ti oxides are reported in Supplementary Data Table A4. Major and trace element analyses of whole-rocks and glasses are reported in Supplementary Data Table A5 along with any whole-rock, glass, and melt inclusion data that are available in the literature and used in this study. Selected whole-rock (Sr, Ba) and plagioclase (FeO, Mg, Sr, Ti, Ba) trace element concentrations are shown in Figs 4 and 5, respectively. Additional plagioclase trace elements are shown in Supplementary Data Fig. A1. Plagioclase trace elements have similar ranges throughout the units: FeO = 0.14–0.47 wt%, Mg = 20–370 ppm, Ti = 40–220 ppm, Mn = 10–110 ppm, Sr = 370–1250 ppm, Zn = 3–14 ppm, Ga = 15–60 ppm, Y < 2 ppm, Rb < 4 ppm, Ba = 90–1300 ppm, Pb = 1–17 ppm, Li = 10–60 ppm, La = 2–14 ppm, Ce = 4–18 ppm, Nd < 5 ppm, and Eu < 4 ppm. In general, contents of the more abundant trace elements, FeO, Mg, Ti, Mn, Sr, Zn, Ga, and Y, increase with increasing An contents, whereas Ba decreases with increasing An contents (Fig. 5, Supplementary Data Fig. A1). There is no apparent relationship between An contents and the remaining trace elements characterized by relatively low concentrations (i.e. Rb, Pb, Nd and Eu).

Isotopic compositions
Whole-rock isotopic ratios
New Sr isotopic analyses for Whakatane, Rotoma, Rotoiti, Kakapiko, Haparangi and Round Hill, and new Pb isotopic data for all units, are listed in Supplementary Data Table A6, along with previously published whole-rock Sr, Nd and Pb isotopic data that have been corrected to the same standard ratios (where possible) and used in this study. Whole-rock isotopic compositions are shown in Fig. 6 (Sr and Pb) and Fig. 7 (Sr only). Except for Rotoiti, all units have similar Sr isotopic ratios, with $^{87}Sr/^{86}Sr_{average} = 0.70534 \pm 0.00003$ (2sd). In general, Rotoiti ratios are lower with $^{87}Sr/^{86}Sr_{average} = 0.70525 \pm 0.00003$ (2SD), although previously published Rotoiti analyses with less radiogenic $^{206}Pb/^{204}Pb$ ratios fall directly within the $^{87}Sr/^{86}Sr_{average}$ of the other units (Fig. 6a). Rhyolite Pb isotopic ratios have $^{207}Pb/^{204}Pb_{average} = 15.641 \pm 0.006$ (2SD) and $^{208}Pb/^{204}Pb_{average} = 38.759 \pm 0.008$ (2SD) but exhibit slight variation in $^{206}Pb/^{204}Pb$ ratios with Rotoiti having less radiogenic ratios (Fig. 6).

Plagioclase isotopic ratios
Overall, whole-crystal Sr isotopic ratios, albeit a small suite, are similar across the units with $^{87}Sr/^{86}Sr_{average} = 0.70528 \pm 0.00019$ ($n = 18$). The intra-caldera, Rotoiti, and Round Hill plagioclase directly overlap with their whole-rock ratios, whereas Earthquake Flat, Kakapiko and Haparangi are slightly ($^{87}Sr/^{86}Sr$ difference = 0.0001) less radiogenic than their whole-rock ratios (Fig. 6a). All whole-crystal plagioclase $^{87}Sr/^{86}Sr$ ratios (solution MC-ICP-MS) are well within the $^{87}Sr/^{86}Sr$ intra-crystal range obtained via LA-MC-ICP-MS (Fig. 7). Whole-crystal Pb isotopic compositions of plagioclase from non-caldera units cluster in Pb–Pb space, whereas
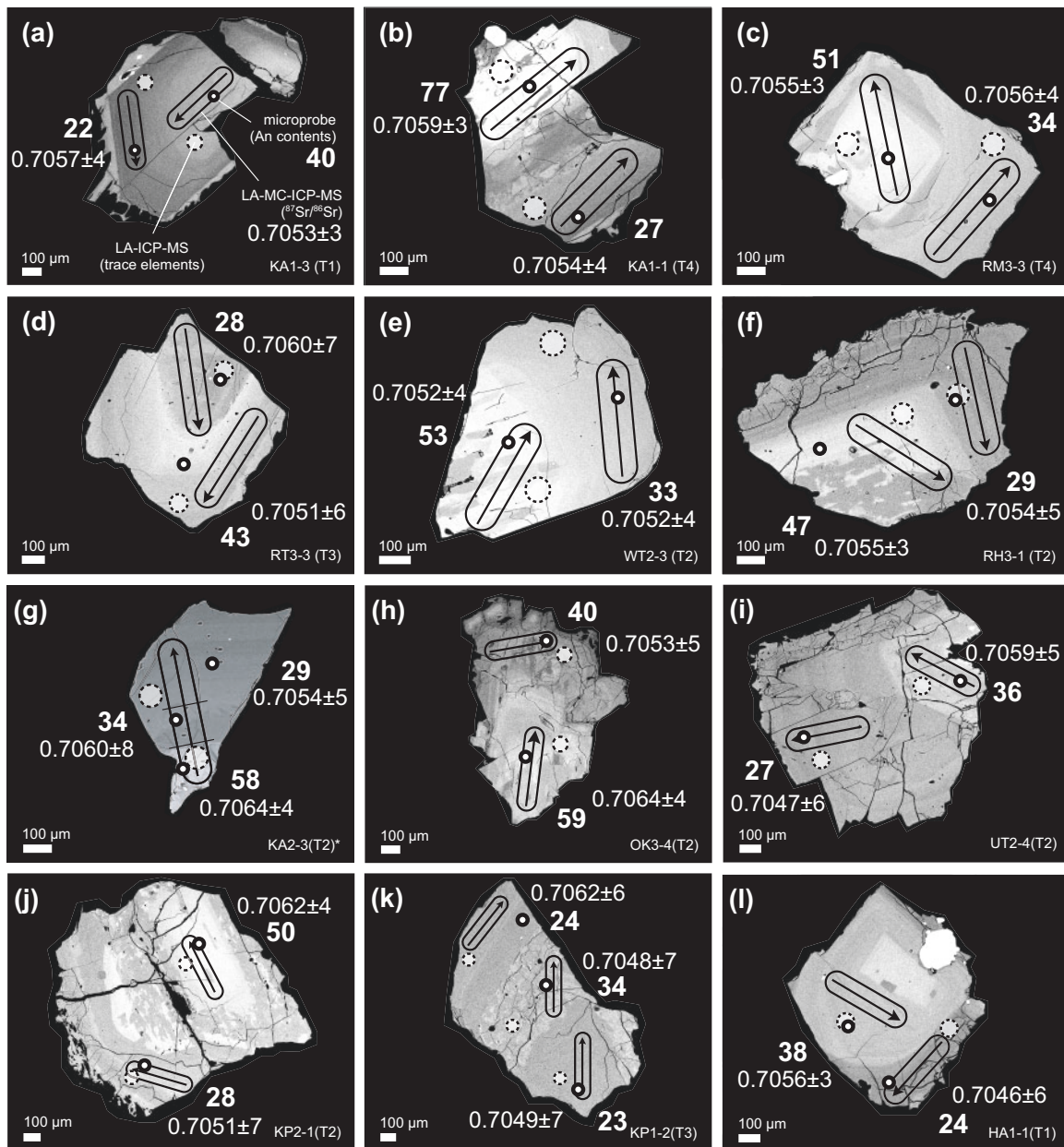
Fig. 3. Back-scattered electron images of representative plagioclase crystals extracted from high-SiO₂ OVC rhyolites. (a–f) Representative plagioclase crystals with homogeneous intra-crystal Sr isotopic ratios. (g–l) All plagioclase crystals with heterogenous intra-crystal Sr isotopic ratios (six out of 115 analyzed). Included in each image are locations of ^{87}Sr/^{86}Sr analysis troughs (LA-MC-ICP-MS; arrows surrounded by black outlines), major and minor element analyses (electron microprobe; small white circles with thick black outlines), trace element analyses (LA-ICP-MS; large white circles with dashed black outlines), and textural group (T1, T2, T3 or T4; Fig. 2). White bars in all images are 100 μm scales. LA-MC-ICP-MS and LA-ICP-MS markers are to scale. The specific crystal label is indicated at the bottom right corner of each image along with the crystal textural group, which is included in parentheses.

plagioclase crystals from the caldera-forming units of Rotoiti and Utu have slightly less radiogenic ^{206}Pb/^{204}Pb ratios (Fig. 6). Whole-rock Pb isotopic ratios cluster even more tightly in Pb–Pb space, with Rotoiti having slightly less radiogenic ^{206}Pb/^{204}Pb ratios (Fig. 6). Whole-crystal and whole-rock Pb isotopic ratios overlap within error, although plagioclase exhibits greater variation (beyond error) in ^{206}Pb/^{204}Pb ratios than whole-rock ratios. There is a discrepancy between previously published rhyolite whole-rock data and whole-rock and plagioclase data obtained in the present study.

However, because the standard ratios used to calibrate the data were not reported in previous studies, published whole-rock Pb isotopic ratios could not be corrected to the standard ratios used in the present study (Supplementary Data Table A6). Whole-crystal plagioclase Sr and Pb isotopic ratios are listed in Supplementary Data Table A3.

Intra-crystal (i.e. core and rim, obtained via LA-MC-ICP-MS) ^{87}Sr/^{86}Sr isotopic ratios of plagioclase range from 0·7042 to 0·7065 (±0·0004 2SE average analytical error; Supplementary Data Table A2). The majority (c.
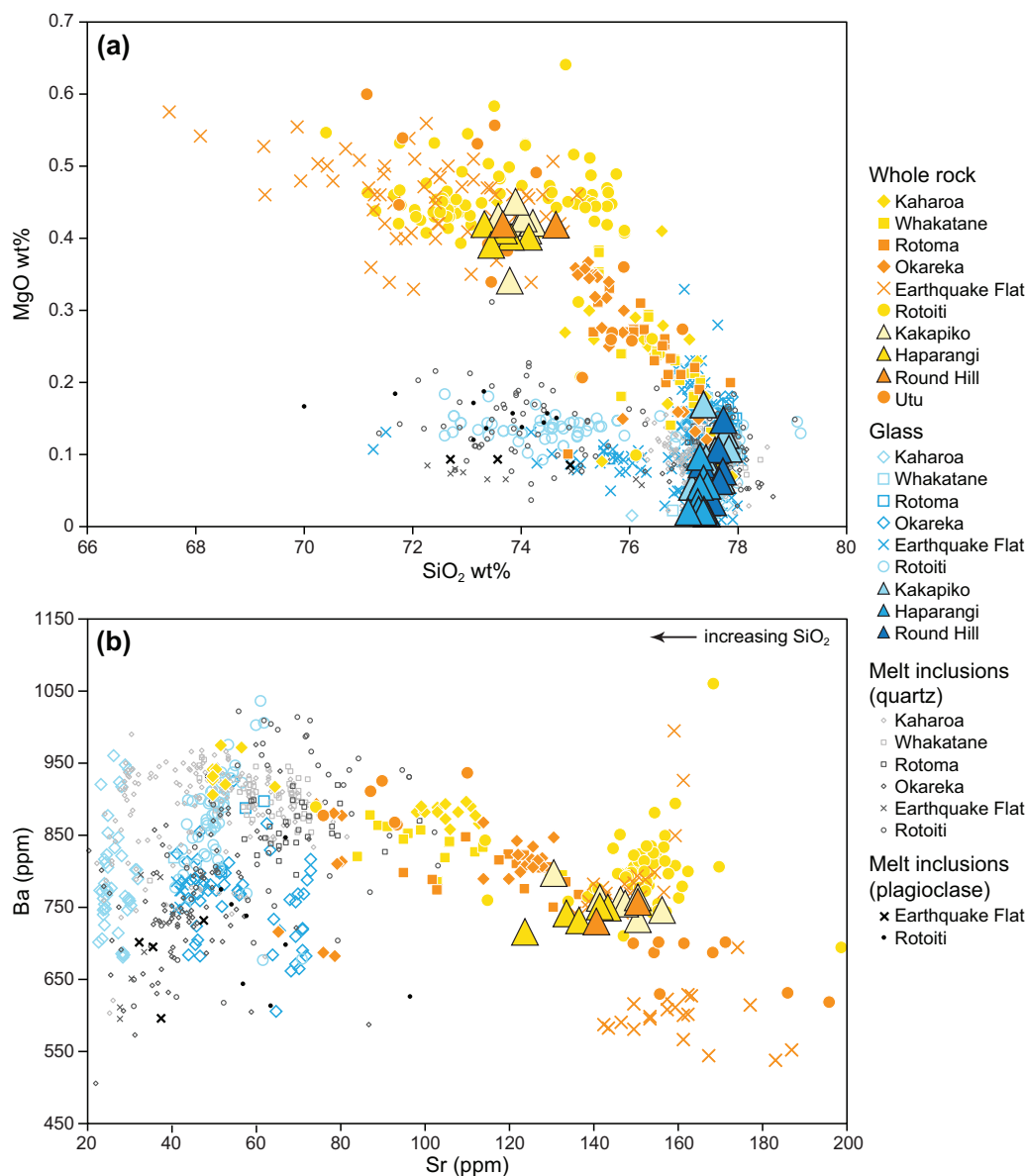
Fig. 4. Whole-rock, glass and quartz- and plagioclase-hosted melt inclusion (a) MgO vs SiO$_2$ and (b) Ba vs Sr. New data include whole-rock and glass compositions for Kakapiko, Haparangi, and Round Hill domes and are marked as large, filled triangular symbols with black outlines. Whole-rock, glass, and melt inclusion compositions and their respective references are listed in Supplementary Data Table A5.

80 %) of ^{87}Sr/^{86}Sr ratios are between 0·7050 and 0·7060 and fall within error, indicating intra-crystal homogeneity (at the resolution in this study, ±0·0004 average 2SE). To test for unitary plagioclase populations in each unit, the intra-crystal ^{87}Sr/^{86}Sr ratios were modelled using kernel density estimates (KDE) and the respective unit mean 2SE analytical error as the bandwidth (Supplementary Data Fig. A2). In each unit, the models output a standard deviation that is roughly double the analytical uncertainty, indicating the presence of isotopic heterogeneity. Isotopic heterogeneity is largely noted as inter-crystal variability within a single unit (i.e. between crystals, noted as core versus core and/or rim versus rim compositions on either side of the ^{87}Sr/^{86}Sr spectrum; Fig. 7). Furthermore, six crystals (out of 115

analyzed) exhibit intra-crystal ^{87}Sr/^{86}Sr ratio variability beyond analytical error (Fig. 3g–l). Intra-crystal isotopic variability in plagioclase is correlated to An contents and is found in crystals that exhibit normal zoning (T1 and T2; Fig. 2). Specifically, in isotopically heterogeneous plagioclase crystals, higher-An zones have more radiogenic ^{87}Sr/^{86}Sr ratios than their respective lower-An zones (Fig. 3g–l). A single exception is Kakapiko plagioclase KP1-2 (Fig. 3k).

DISCUSSION

Controls on plagioclase composition

When coupled with textures, variable plagioclase An contents indicate at least two important growth phases.
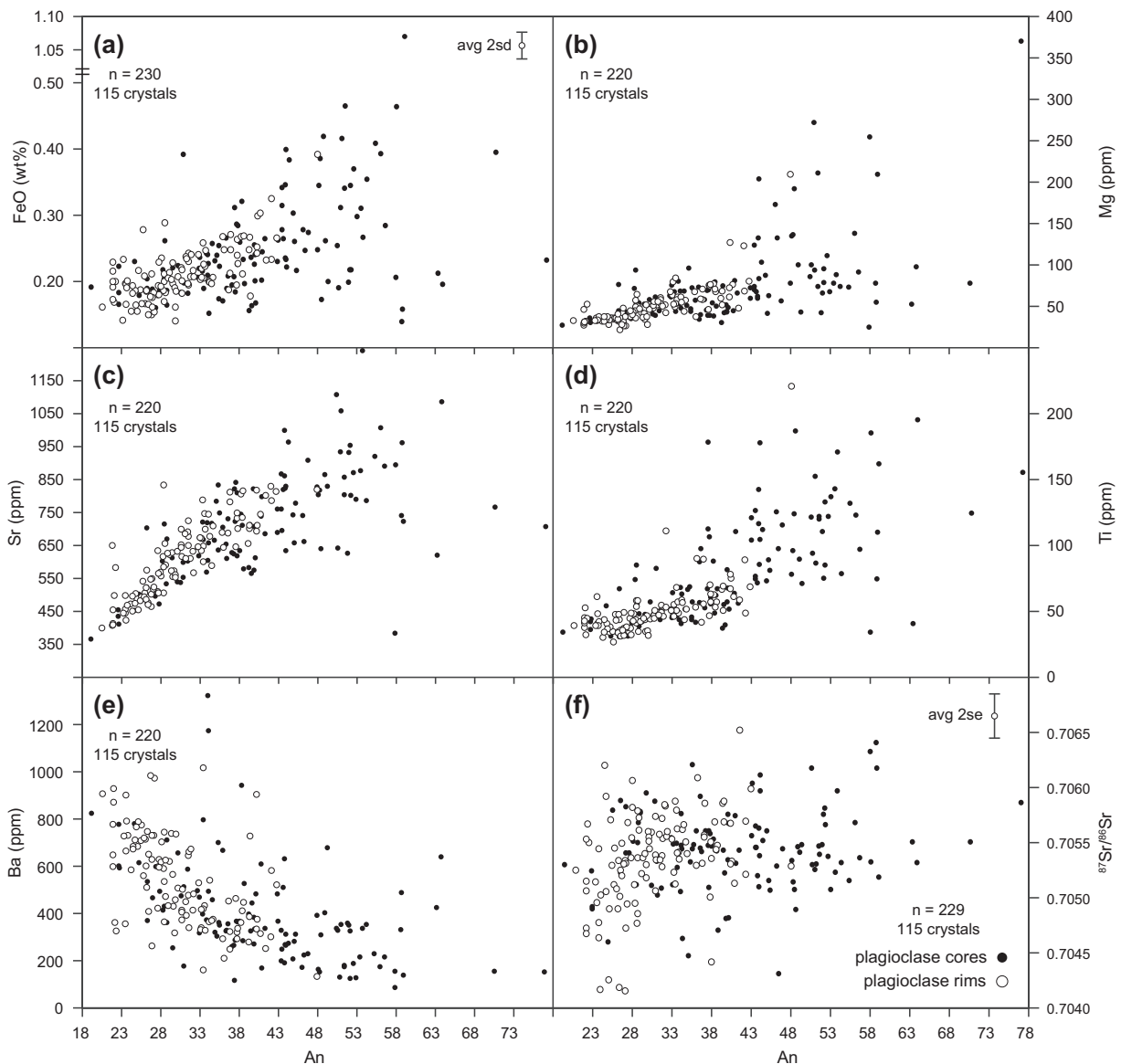
Fig. 5. Selected plagioclase trace element concentrations and intra-crystal $^{87}Sr/^{86}Sr$ ratios vs An contents. Error bars for trace elements obtained via LA-ICP-MS (Mg, Sr, Ti, Ba; b–e) are equivalent to or smaller than their respective symbols. Filled black symbols represent plagioclase cores, and open symbols represent plagioclase rims. Plagioclase major element analyses are listed in Supplementary Data Table A1, and LA-ICP-MS and LA-MC-ICP-MS analyses are listed in Supplementary Data Table A2.

The earlier history of crystallization is represented by variable An contents and resorption textures observed in cores and reversely zoned crystals. The second growth phase relates to the omnipresence of normally zoned, relatively low-An outermost crystal rims (Fig. 3; Supplementary Data Table A1). The ubiquity of resorption textures in plagioclase interiors, also previously observed for Kaharoa by Shane (2015), indicates periods of disequilibrium in the 10 OVC units investigated here. Resorption of higher-An cores (T2 and T4; Figs 2 and 3) found throughout the units is characterized by a boxy-cellular texture, which is thought to represent recrystallization following dissolution (Streck, 2008, and references therein). The An variations (commonly ΔAn ≈ 20; Sas *et al.*, 2019) between the different domains of boxy-cellular cores indicate that they were not in

equilibrium with the surrounding melt. Decompression is considered as a possible cause, but is more likely to result in spongy textures (Nelson & Montana, 1992). Alternatively, the boxy-cellular texture could result from further crystallization in water-saturated magmas (Blundy & Cashman, 2001). Dissolution is also noted in plagioclase crystals that exhibit reverse zoning between crystal cores or mantles and rims (T3 and T4; Figs 2 and 3). However, the outermost normally zoned rims observed in plagioclase from all units lack dissolution textures and suggest late-stage equilibrium crystallization in a fractionating melt, as previously noted by Shane (2015).

It has been suggested that the relationship between trace element concentrations and An contents of the plagioclase in OVC magmas is mostly controlled by the
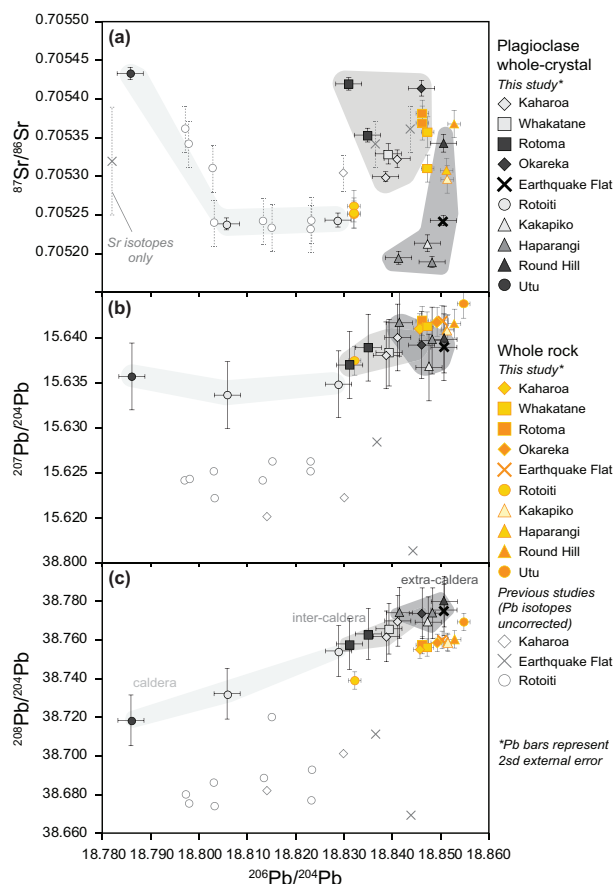
Fig. 6. Newly obtained isotopic compositions of OVC plagioclase (gray symbols) and high-SiO$_2$ rhyolite whole-rocks (orange and yellow symbols), and previously published whole-rock (pale gray symbols). OVC whole-crystal plagioclase isotopic ratios are listed in Supplementary Data Table A3. New whole-rock Sr and Pb isotopic ratios are listed in Supplementary Data Table A6 along with previously published whole-rock isotopic ratios and their respective references. The systematic offset between plagioclase and whole-rock ^{208}Pb/^{204}Pb ratio stems from the uncertainty in the calibration line (Supplementary Data Table A3), which affects all plagioclase measurements equally. Relative precision between plagioclase analyses is not affected by this uncertainty.

melt compositions (Smith *et al.*, 2010; Shane, 2015). This is supported here for a wider selection of OVC magmas. The lower concentrations of Fe, Mg, Sr and Ti with lower An contents (Fig. 5) imply depletion of these respective elements within the host melt as they are incorporated into crystallizing phases. For instance, a decrease in Ti contents with decreasing An content is consistent with fractional crystallization trends caused by incorporation of Ti into Ti-rich phases such as amphibole, biotite, and Fe–Ti oxides (Patiño Douce, 1993; Ernst & Liu, 1998). Additionally, as both Fe and Mg also decrease with An decrease, it is unlikely that Fe variations are a result of fO_2 changes (Shane, 2015), and instead they result from compositional changes within the host magma as the two elements are incorporated into ferromagnesian phases such as biotite, amphibole, and pyroxene (Ginibre *et al.*, 2002). Importantly, although Mg and Fe exhibit a positive

correlation with one another and a negative correlation with An, there is a wide scatter in Mg and Fe contents at high An (i.e. in plagioclase cores) (Fig. 5a and b). This is likely to be an effect of post-crystallization diffusion, as Mg is highly mobile (Costa *et al.*, 2003). Some scatter is also noted in Sr contents at higher An (Fig. 5c) but is less pronounced. Strontium diffuses more slowly than Mg and Fe in plagioclase, and therefore we infer it to represent either fluctuations in melt composition or minor Sr diffusion in some plagioclase cores (i.e. full diffusion would result in Sr increase with An decrease; Zellmer *et al.*, 1999, 2003). In contrast, Ti diffuses slowly in plagioclase (Humphreys, 2011), therefore we interpret variations in Ti contents (Fig. 5d) to be melt-controlled. The high Ti in most of the plagioclase cores indicates crystallization from higher-Ti melts. We infer that these melts are more mafic in composition based on the higher Ti contents of more mafic TVZ magmas (e.g. Gamble *et al.*, 1993; Leonard *et al.*, 2002; Nairn, 2002; Schmitz & Smith, 2004).

We interpret OVC plagioclase cores to be of antecrystic origin (i.e. relics from forerunner magmatism but not that of the host rock) based on (1) reverse zoning textures, (2) variable trace element contents relative to An, and (3) evidence for diffusional control on some of the Mg and Fe contents. The elevated Ti contents of plagioclase cores reflect origins from variable, more mafic melts. Cores are interpreted to be antecrysts and not xenocrysts based on high An contents (surrounding metasedimentary plagioclase is sodic with An$_{<50}$; Price *et al.*, 2012), size (cores are typically ≫200 μm, whereas metasedimentary minerals are <200 μm; Price *et al.*, 2015), and, as discussed below, isotopic ratios. In contrast, plagioclase rim growth is probably controlled via fractional crystallization. This interpretation is based on the good Fe–Mg correlation of plagioclase rims, which indicate melt-driven compositional changes (Shane, 2015).

Plagioclase–melt equilibrium

Equilibrium melt compositions using plagioclase molar Ca/Na ratios and Sr contents (Supplementary Data Tables A1 and A2, respectively) were modelled and compared with available whole-rock, glass, and melt inclusion compositions (Supplementary Data Table A5 and references therein) to test whether the crystals are cognate with their carrier magma. The plagioclase and melt partition coefficient ($K_{Ca/Na}$) is robustly known and increases with H$_2$O content and to a lesser extent with pressure (Sisson & Grove, 1993; Lange *et al.*, 2009). Thus equilibrium between OVC plagioclase crystals and their carrier magmas was evaluated using experimentally determined $K_{Ca/Na}$ of Sisson & Grove (1993) and Martel *et al.* (2006) and water contents based on melt inclusion data (Fig. 8; Table 2). For >45 ka units, where water content data are lacking, values from Earthquake Flat deposits (Smith *et al.*, 2010) were assumed because of similar petrography and geochemistry to the older units (Tables 1 and 2, Fig. 4). Pressure is not a concern
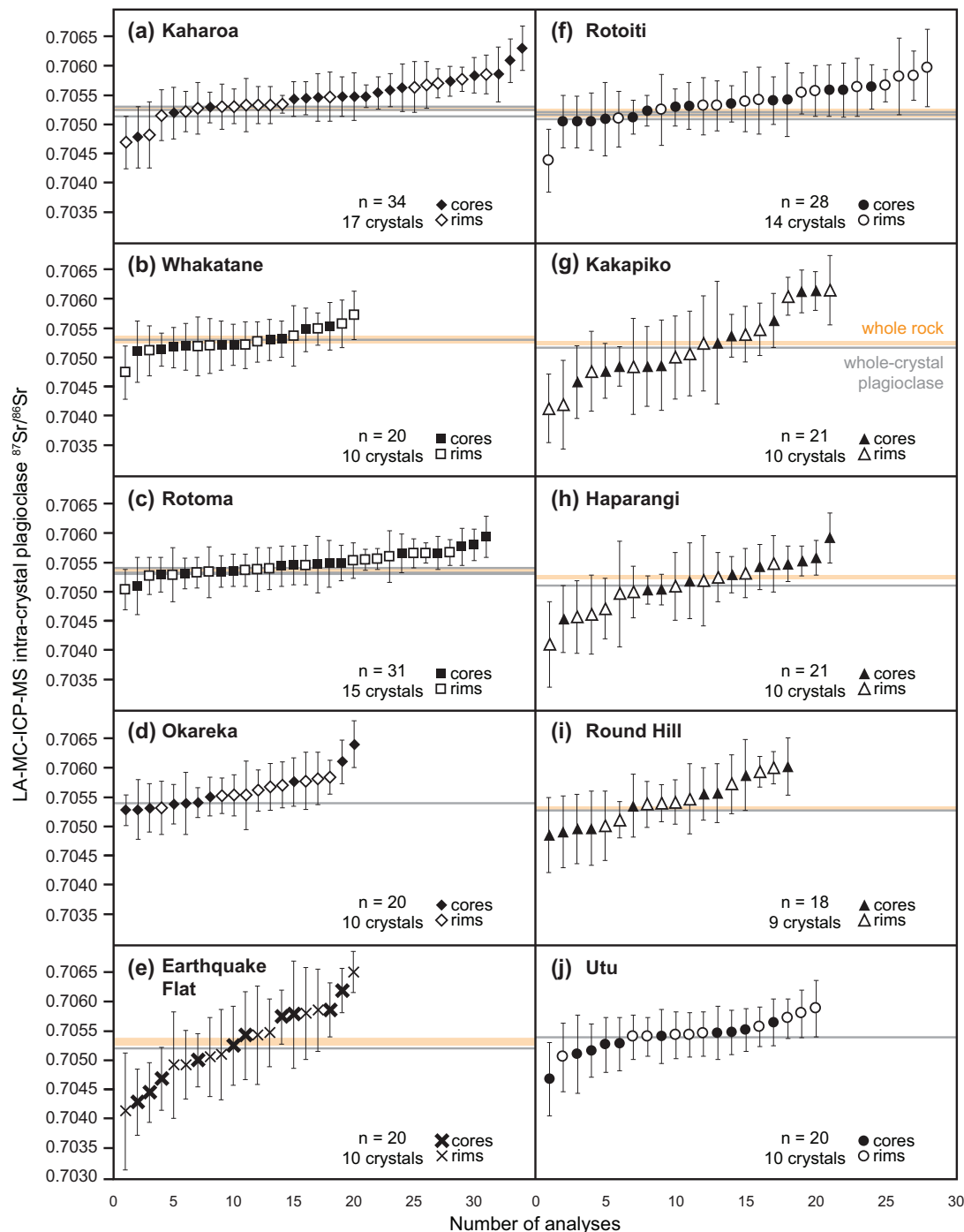
Fig. 7. Per-unit plagioclase intra-crystal $^{87}Sr/^{86}Sr$ ratios, sorted in increasing order, with cores shown as filled black symbols and rims as open symbols. Whole-crystal $^{87}Sr/^{86}Sr$ ratios (Supplementary Data Table A3) are shown as gray lines and whole-rock $^{87}Sr/^{86}Sr$ ratios (Supplementary Data Table A6) are shown as orange lines.

for OVC plagioclase compositions owing to the probably low, minimally varying magma pressures (Table 1).

The Ca/Na ratios of plagioclase rims in most OVC deposits have a limited range (within <1), suggesting nucleation from fairly uniform melt(s) (Fig. 8). To assess potential equilibrium, overlaps between plagioclase rims and potential host melt Ca/Na ratios were examined relative to $K_{Ca/Na}$ (Fig. 8). If equilibrium was

assumed with glass or melt inclusion compositions, which have similar Ca/Na ratios, plagioclase rim Ca/Na ratios imply crystallization from hydrous melts (≥3 wt% H_2O). If the whole-rock composition is assumed to be the equilibrium melt, then plagioclase rim Ca/Na ratios for the intra-caldera (Kaharoa, Whakatane, Rotoma and Okareka) and caldera (Rotoiti and Utu) units also indicate hydrous melts (≥3 wt% H_2O), whereas the rest of the units indicate less hydrous to dry conditions (mostly
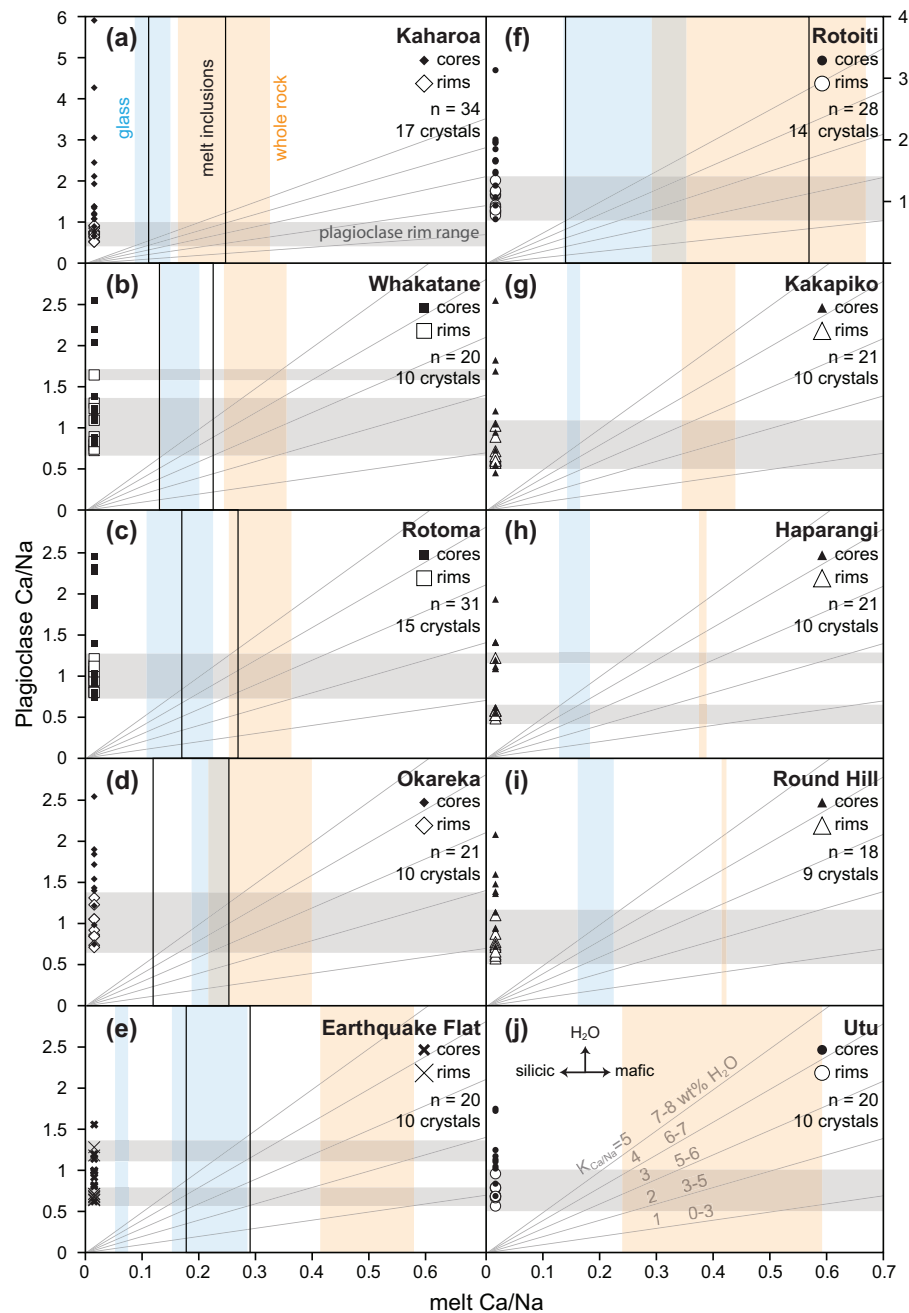
Fig. 8. Molar Ca/Na ratios of plagioclase cores and rims plotted against their potential host melt molar Ca/Na ratios, where host melts are represented by whole-rock, glass, and melt inclusion Ca/Na ratios. Plagioclase cores are shown as filled black symbols and plagioclase rims are shown as open symbols (rim range is also shown as horizontal gray regions) (Supplementary Data Table A1). Shaded orange regions represent the range of whole-rock Ca/Na, blue shaded regions represent the range of glass Ca/Na, and the black lines represent the range of melt inclusion Ca/Na (whole-rock, glass, and melt inclusion compositions, and their respective references, are listed in Supplementary Data Table A5). Equilibrium is implied where the vertical and horizontal regions cross. Diagonal gray lines represent partition coefficients ($K_{Ca/Na}$) between plagioclase and melt and are indicative of H_2O contents in the respective melt (Martel *et al.*, 2006), with $K_{Ca/Na} = 5$ being the maximum in natural samples.

≤ 3 wt% H_2O). High H_2O contents of *c.* 5 wt% (Table 2) are consistent with melt inclusion data (Smith *et al.*, 2010; Johnson *et al.*, 2011, 2013) and the presence of biotite and/or amphibole (Table 1). Because respective glass and melt inclusion Ca/Na ratios indicate more hydrous conditions (Fig. 8), they are likely to be more representative of the host melts rather than the whole-rock

compositions. However, we note that for caldera and intra-caldera units, whole-rock compositions are also potential representative parental melts for plagioclase rims (Fig. 8).

The Ca/Na ratios of plagioclase cores reveal a different story. For all units, Ca/Na ratios of plagioclase cores span a wider range than that of the rims and include

very high ratios (Fig. 8). For some crystals, the observed Ca/Na ratios (overlapping plagioclase and potential melt regions that fall above $K_{Ca/Na} = 5$) would exceed H_2O contents of natural rhyolitic samples (Martel *et al.*, 2006). Thus, fluctuations in H_2O contents alone cannot explain the Ca/Na ratio variability observed in all plagioclase cores. As a result, we infer this variability to reflect nucleation in compositionally discrete melts with differing CaO contents (i.e. more mafic, as also suggested by Ti contents of plagioclase cores).

We utilized trace element (Sr) concentration models to further explore potential parental melt compositions for the plagioclase interiors (Model III of Dohmen & Blundy, 2014; Supplementary Data Materials, Supplementary Data Fig. A3). Model inputs consisted of (1) individual plagioclase compositions (Supplementary Data Table A2; each analysis was modelled), (2) the respective unit average whole-rock, glass, or melt inclusion SiO_2 contents (Table 2; each average was modelled separately for each unit), and (3) the respective unit average temperatures calculated using Fe–Ti oxides (Table 1; Supplementary Data Materials). Models using melt inclusion SiO_2 contents yielded the same results as models using matrix glass SiO_2 contents, therefore the modelling results for the two are presented together in Fig. 9. Plagioclase–melt K_{Sr} values are listed in Supplementary Data Table A2, and Sr contents of the modelled melts are shown in Fig. 9. Because units with ages >45 ka (Kakapiko, Haparangi, Round Hill, Utu) do not have available Sr contents for glass and melt inclusions, Earthquake Flat glass and melt inclusion Sr contents were used as a reference (based on petrographic and geochemical similarities between the units; Tables 1 and 2, Fig. 4), but were not used to assess equilibrium.

Concentrations of Sr in the modelled melts are similar across the units (Sr $\approx$ 50–170 ppm, rarely >200 ppm). For all units, modelled melts show an increase in Sr contents with higher An (Fig. 9). Overall, modelled melt compositions rarely overlap with their matrix glass Sr contents, indicating that the glass compositions are not ideal parental melt compositions for OVC plagioclase. Calcic plagioclase ($An_{>45}$; cores) produces more heterogeneous modelled melt compositions when viewed as a suite. For Utu (Fig. 9j), calcic plagioclase could have crystallized in host melt compositions like that of the whole-rock (and consistent with Ca/Na ratios). For the rest of the units, calcic cores have higher Sr contents than their respective whole-rock, glass, or melt inclusion compositions. This indicates that calcic plagioclase cores are derived from more mafic melts (i.e. melt with higher Sr contents). However, OVC basalts have higher Sr contents than calcic plagioclase cores (e.g. Gamble *et al.*, 1993; Leonard *et al.*, 2002; Schmitz & Smith, 2004). This indicates that plagioclase cores are not direct relics from basaltic melts and instead crystallized from intermediate melts. In contrast, sodic plagioclase ($An_{<45}$; rims) produces modelled melts with less variability. For Rotoiti and the

intra-caldera units (Kaharoa, Whakatane, Rotoma, Okareka), modelled melt compositions for sodic plagioclase overlap with whole-rock and/or melt inclusion compositions (Fig. 9a–d, and f), which suggests that (along with Ca/Na ratios) the plagioclase is cognate with their carrier magma.

Plagioclase isotopic compositions

We acknowledge some limitations of intra-crystal $^{87}Sr/^{86}Sr$ analyses in this study: (1) low ^{88}Sr voltage (<1) owing to laser operation and/or beam diameter (65–100 μm) limits the precision ($\pm$0·0004 average 2SE) of the analysis; (2) the Sr isotopic ratio is a homogenization of the signal where laser tracks cut across unrecognized compositional domains; (3) some compositional domains may have been too small to be isolated by the beam diameter used. Thus, isotopic heterogeneity may be greater than that detected. At the precision obtained, the majority (*c.* 80 %) of intra-crystal Sr isotopic ratios are within error of their respective whole-crystal Sr isotopic ratios. The general lack of isotopic variation at intra-crystal-scale in the samples examined implies crystallization from a common isotopic source that has not varied significantly in the last *c.* 550 kyr (Fig. 7, Supplementary Data Table A2). However, we do note that a few calcic plagioclase cores have $^{87}Sr/^{86}Sr$ ratios that are more radiogenic than their respective sodic rims, indicating some diversity in melts (Fig. 3g–l).

The more precisely determined whole-crystal and whole-rock Sr and Pb isotopic ratios cluster tightly in Sr–Pb space and are more radiogenic than TVZ basalts (Supplementary Data Fig. A4). In Pb–Pb space, newly obtained Pb ratios for OVC plagioclase and rhyolites differ from previously published ratios for OVC rhyolites (Fig 6). However, the reported ratios could not be corrected to the standard ratios used in the present study because standard ratios were not reported in the previous studies (Supplementary Data Table A6). Furthermore, the majority of samples (Graham *et al.*, 1992; Schmitz & Smith, 2004) were not double-spiked, significantly reducing the precision of these previous Pb isotopic analyses (Woodhead *et al.*, 1995; Taylor *et al.*, 2015). Relative to surrounding mid- to upper crust, Sr isotopic ratios of OVC plagioclase are not as radiogenic as the majority of Torlesse Terrane metasediments, and Pb isotopic ratios are mostly too radiogenic to be sourced from Waipapa Terrane metasediments. Based on the isotopic ratios of OVC plagioclase, as well as core compositions that indicate more mafic (albeit non-basaltic) origins, we suggest that plagioclase crystals nucleated in intermediate melts formed by mixing between basalts and crustal melts and/or fractional crystallization of basalts that have undergone significant crustal assimilation prior to fractionation.

Because plagioclase and whole-rock isotopic ratios indicate significant crustal contamination, assimilation–fractional crystallization (AFC) and mixing models were completed in an effort to reproduce the observed OVC
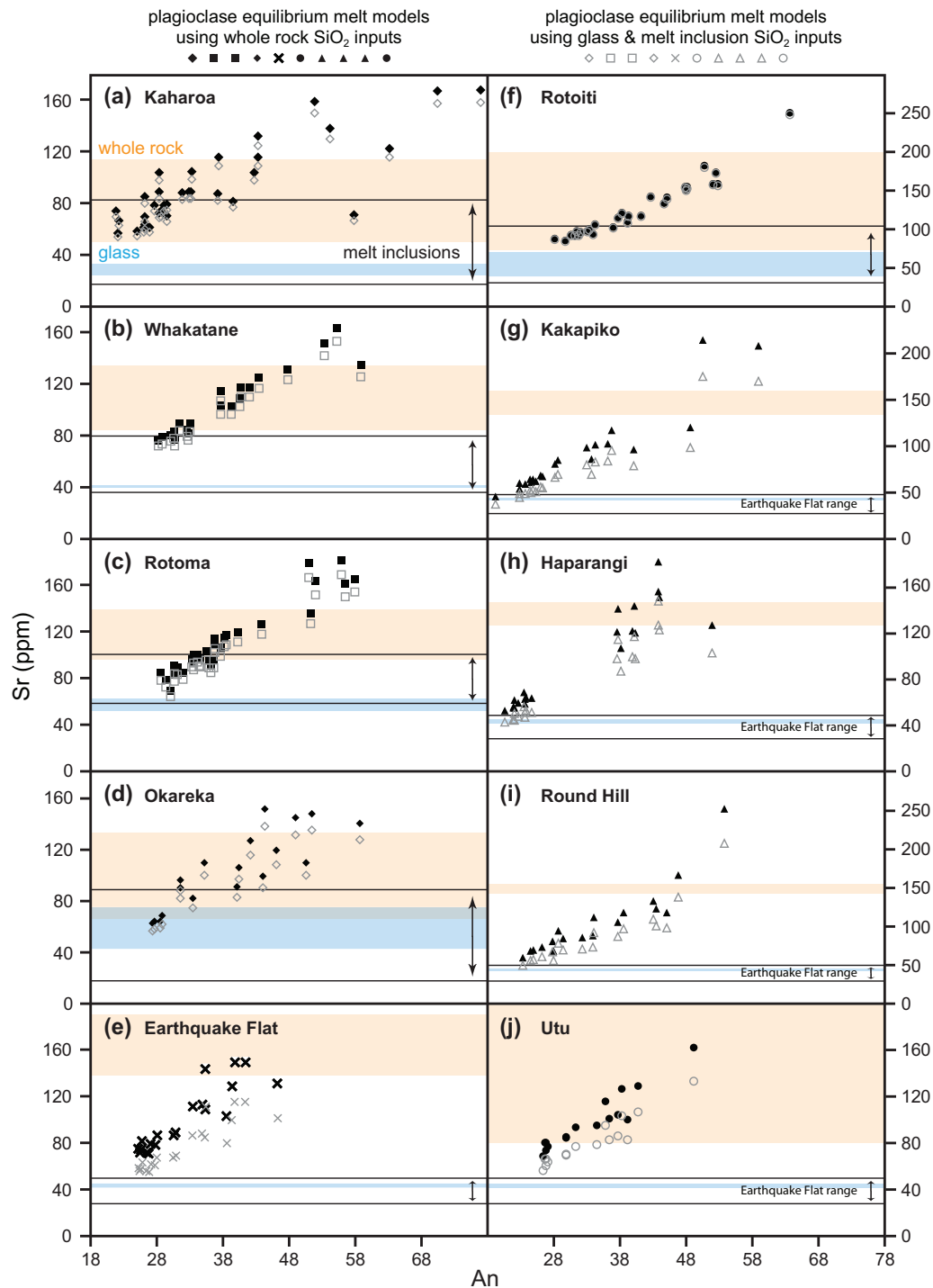
Fig. 9. Plagioclase Sr equilibrium melts, calculated using K_{Sr} of Dohmen & Blundy (2014) (plagioclase Sr contents and K_{Sr} are included in Supplementary Data Table A2), vs plagioclase An contents (Supplementary Data Table A1). Filled black symbols represent equilibrium melts calculated using whole-rock SiO_2 contents, and gray symbols represent equilibrium melts calculated using glass and melt inclusion SiO_2 contents. Shaded orange regions represent the range of whole-rock Sr contents, blue shaded regions represent the range of glass Sr contents, the black lines with the arrow represent the range of melt inclusion Sr contents (whole-rock, glass, and melt inclusion compositions, and their respective references, are listed in Supplementary Data Table A5).

isotopic ratios and whole-rock compositions (Figs 11–13). Numerous possibilities were considered for mantle sources of parent basalts (all known Zealandia mantle sources), dominant crustal assimilants (Torlesse and Waipapa Terranes), and additional crustal contaminants

(TVZ metaigneous and metasedimentary xenoliths) (all shown in Supplementary Data Fig. A4; data and references are included in Supplementary Data Table A6). Unfortunately, Sr–Nd–Pb isotopic compositions of TVZ mantle sources are poorly constrained as erupted TVZ
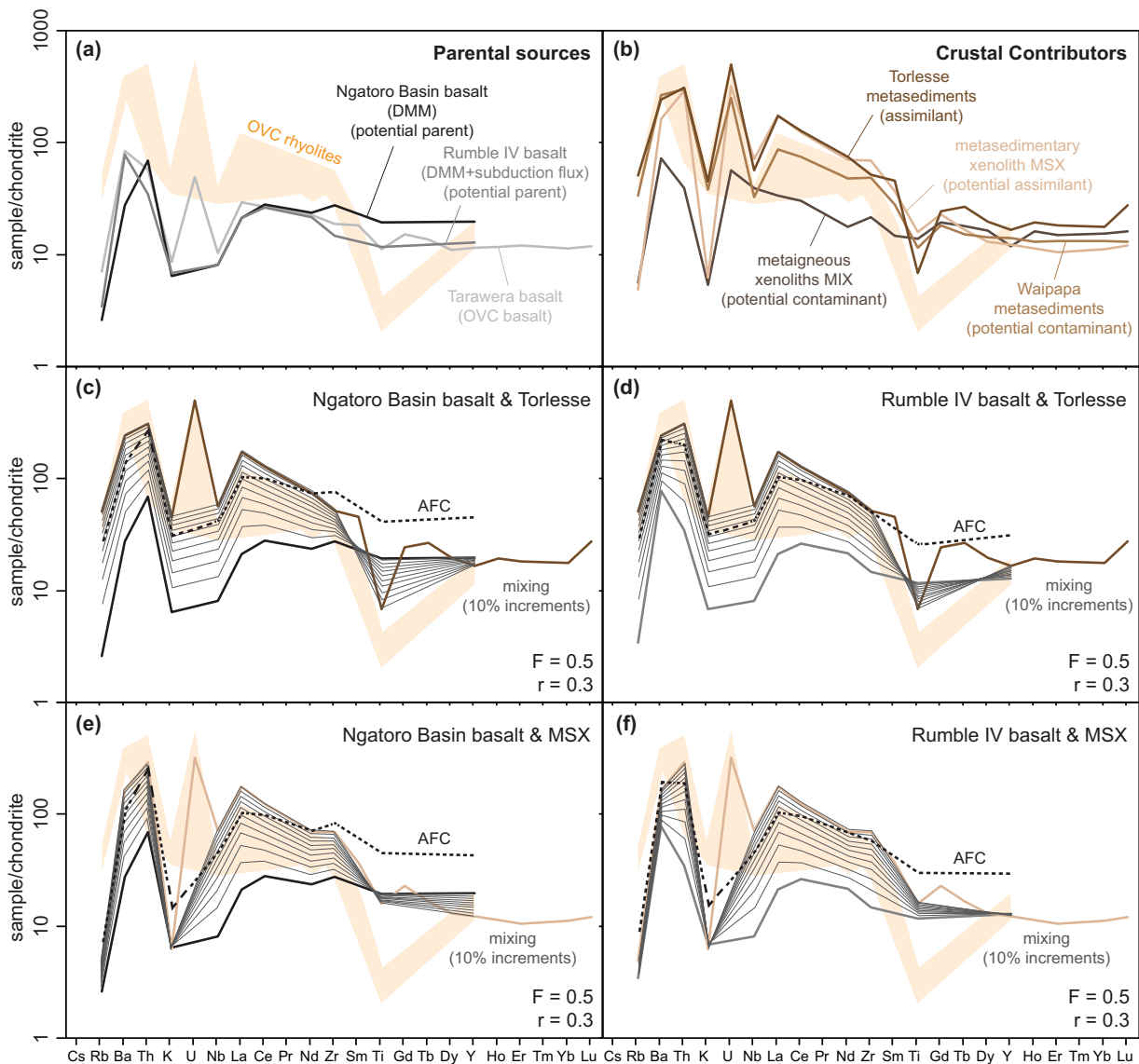
Fig. 10. Compositional results of AFC models (dashed lines) and mixing models (thin, sequential gray lines) using offshore TVZ basalts as parents and TVZ regional metasediments as assimilants vs OVC rhyolite whole-rock compositions (orange shaded regions). (a) Compositions of potential parental melts. (b) Compositions of potential crustal assimilants and contaminants. (c, d) Modeling results of parental melts and Torlesse metasediments as the assimilant. (e, f) Modeling results of parental melts and a Torlesse-like metasedimentary xenolith from the southern TVZ with more enriched Pb isotopic ratios as the assimilant. All modeling inputs and representative compositions are listed in Table 3.

basalts have crustally contaminated radiogenic ratios that overlap with TVZ rhyolites. However, recent studies examining compositional and Hf and U isotopic variability between inter-and intra-caldera TVZ basalts have greatly illuminated the compositional differences between the mantle sources from which TVZ primitive magmas are derived (Waight *et al.*, 2017; Barker *et al.*, 2020; Zellmer *et al.*, 2020). These studies call on a highly fractionated (20–30 %) depleted mid-ocean ridge mantle (DMM) source that has experienced slight slab flux for intra-caldera basalts, and a less fractionated (3–10 %) DMM or an enriched mantle source for inter-caldera basalts. Thus, two possible offshore TVZ basalts were modelled as potential parental melts and their compositions are listed in Table 3. The first is a basalt from

Ngatoro Basin in the Havre Trough with a DMM source (sample VUW158/4; Gamble *et al.*, 1993, 1996; Macpherson *et al.*, 1998). The second is a basalt from Rumble IV with a DMM source that was slightly modified by a fluid-dominant subduction flux (sample VUW 162/1; Gamble *et al.*, 1993, 1996; Macpherson *et al.*, 1998). Based on previous TVZ studies, Torlesse metasediments were modelled as the dominant assimilant (McCulloch *et al.*, 1994; Macpherson *et al.*, 1998; Charlier *et al.*, 2008; Price *et al.*, 2012). The Torlesse composition used for modeling is the estimated Torlesse Kaweka composition from Price *et al.* (2015) (Table 3).

Modeling results are shown in Figs 10–12. Models with $r = 0.3$ (based on McCulloch *et al.*, 1994; Price *et al.*,

2012) at 50 % crystallization suggest that a subduction-modified DMM basalt (Rumble IV) and Torlesse metasediments represent reasonable starting AFC endmembers, but Pb isotopic trends of OVC rhyolites and plagioclase require either complete mixing with a Torlesse endmember, which is not feasible based on whole-rock compositions and Sr–Nd isotopic ratios (Fig. 11), or a crustal source that has more radiogenic $^{207}Pb/^{204}Pb$ and $^{208}Pb/^{204}Pb$. Therefore, a second assimilant—a southern TVZ metasedimentary xenolith (MSX) with more radiogenic $^{207}Pb/^{204}Pb$ and $^{208}Pb/^{204}Pb$ (sample R97/104A; Price *et al.*, 2012, 2015)—was modelled as a potential assimilant. Such metasedimentary xenoliths have been interpreted to be high-grade regional Torlesse or Waipapa metasediments (Price *et al.*, 2012), and could be more representative of mid-crustal metasediments. Although it is not known whether the MSX is of Waipapa or Torlesse origins, except for a K depletion, the MSX is compositionally comparable with the estimated Torlesse metasediment composition used for modelling (Fig. 10b). Consequently, compositional AFC modelling outputs are similar for both the representative Torlesse assimilant and the MSX assimilant. However, owing to the more radiogenic Pb isotopic ratios, the MSX represents a more ideal isotopic endmember. With the MSX as the assimilant and Rumble IV as the parent, OVC rhyolites and plagioclase isotopic ratios can be reproduced reasonably well for non-caldera units and indicate ≥20 % assimilation (Figs 11 and 12).

One issue is variation in plagioclase $^{206}Pb/^{204}Pb$ ratios of the OVC caldera-forming units Utu and Rotoiti, which have the least radiogenic $^{206}Pb/^{204}Pb$ ratios of the units (Fig. 6). Several sources should be considered as possible causes for the variation. The first is Waipapa metasediments; however, plagioclase Pb isotopes require a crustal source that is more radiogenic than the known Waipapa range, specifically for $^{207}Pb/^{204}Pb$ and $^{208}Pb/^{204}Pb$ (Fig. 12). The second is incorporation of heterogeneous mantle components, as a heterogeneous mantle has been suggested for TVZ basalt origins (Waight *et al.*, 2017; Barker *et al.*, 2020; Zellmer *et al.*, 2020). However, many Zealandia mantle sources are significantly more enriched in $^{206}Pb/^{204}Pb$ and would drive ratios away from those observed in Rotoiti and Utu (e.g. Auckland Volcanic Field, South Island, Chatham Islands; Huang *et al.*, 1997; Timm *et al.*, 2010), or fall along mixing trends between Havre Trough basalts and regional metasediments and thus would not produce the necessary Pb isotopic trends (e.g. some Northland basalts; Huang *et al.*, 2000) (Supplementary Data Fig. A4). The third is metaigneous xenoliths (MIX in Figs 10–12) that have been found in andesites from the Tongariro Volcanic Centre in the southern TVZ (Graham *et al.*, 1990; Price *et al.*, 2012). These metaigneous xenoliths are derived from hydrothermally altered oceanic crust that underlies the Torlesse metasediments and are thought to represent deep crust compositions below the TVZ (Graham *et al.*,

1990; Price *et al.*, 2005, 2012; Waight *et al.*, 2017). However, known $^{207}Pb/^{204}Pb$ and $^{208}Pb/^{204}Pb$ ratios of metaigneous xenoliths are not radiogenic enough relative to $^{206}Pb/^{204}Pb$ to produce the trends observed in Utu and Rotoiti (Fig. 12) and also have $^{143}Nd/^{144}Nd$ that conflict with those of OVC rhyolites (Fig. 11). Alternatively, the mantle sources associated with magma production of large-volume eruptions represent periods of high DMM decompression melting (e.g. Zellmer *et al.*, 2020). Specifically, the mantle source for these large-volume eruptions contains little to no subduction flux (Macpherson *et al.*, 1998) and would drive trends towards less radiogenic $^{206}Pb/^{204}Pb$ (i.e. more Ngatoro Basin-like, Fig. 12). This scenario would require ≥30 % assimilation of an MSX-like crustal component. Another possibility remains—an unknown lower crust composition is ultimately responsible for the peculiar Pb isotopic trends of OVC rhyolites and plagioclase.

Magmatic model for the OVC

The compositional heterogeneity and textures observed in plagioclase cores are significant because they indicate that they nucleated from different melts. Specifically, the variable Ca/Na ratios of plagioclase cores within a single unit cannot be explained via H_2O fluctuations alone (Fig. 8), and require origins from different, more mafic (although not basaltic) melt compositions. This is supported by trace element contents (e.g. Ti, Fig. 5d) and melts modelled from Sr contents in plagioclase (Fig. 9) that reveal a wide range of melt compositions for calcic cores relative to the narrower range of the sodic rims. In contrast, sodic plagioclase rims indicate late-stage growth in cooler, fractionating melts of more uniform compositions. For caldera and intra-caldera units, these late-stage homogeneous melts are similar to the melt inclusion and/or whole-rock compositions (Figs 8 and 9). Extraction of cores from various melts, and fractional crystallization prior to eruption, are observed across small- and large-volume OVC deposits, emphasizing the importance of these processes at this volcanic centre.

The pre-eruption transport of crystal cores from various sources is demonstrated in previous studies and explains the compositional and thermal diversity of amphiboles (Shane & Smith, 2013), zircon age diversity (e.g. Storm *et al.*, 2011, 2012, 2014), and plagioclase textures and compositions (Shane, 2015). Transportation of crystals could result from convective self-mixing (e.g. Couch *et al.*, 2001). Indeed, localized mixing owing to buoyancy instabilities at OVC has been suggested in numerous studies (Leonard *et al.*, 2002; Nairn *et al.*, 2004; Shane *et al.*, 2005, 2008a; Molloy *et al.*, 2008; Storm *et al.*, 2011). The underplating basaltic magmas that are inferred as the heat source for convection also serve as parental melts that undergo AFC to form the more evolved melts (e.g. Price *et al.*, 2005, 2012; Shane, 2015; Wilson & Charlier, 2016). The intruding basalts regularly recharge and rejuvenate the magmatic system. This is
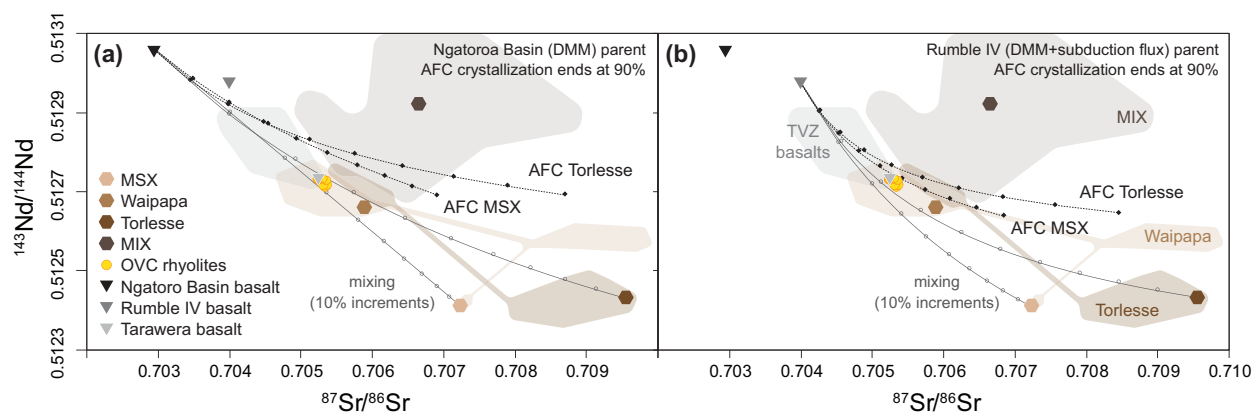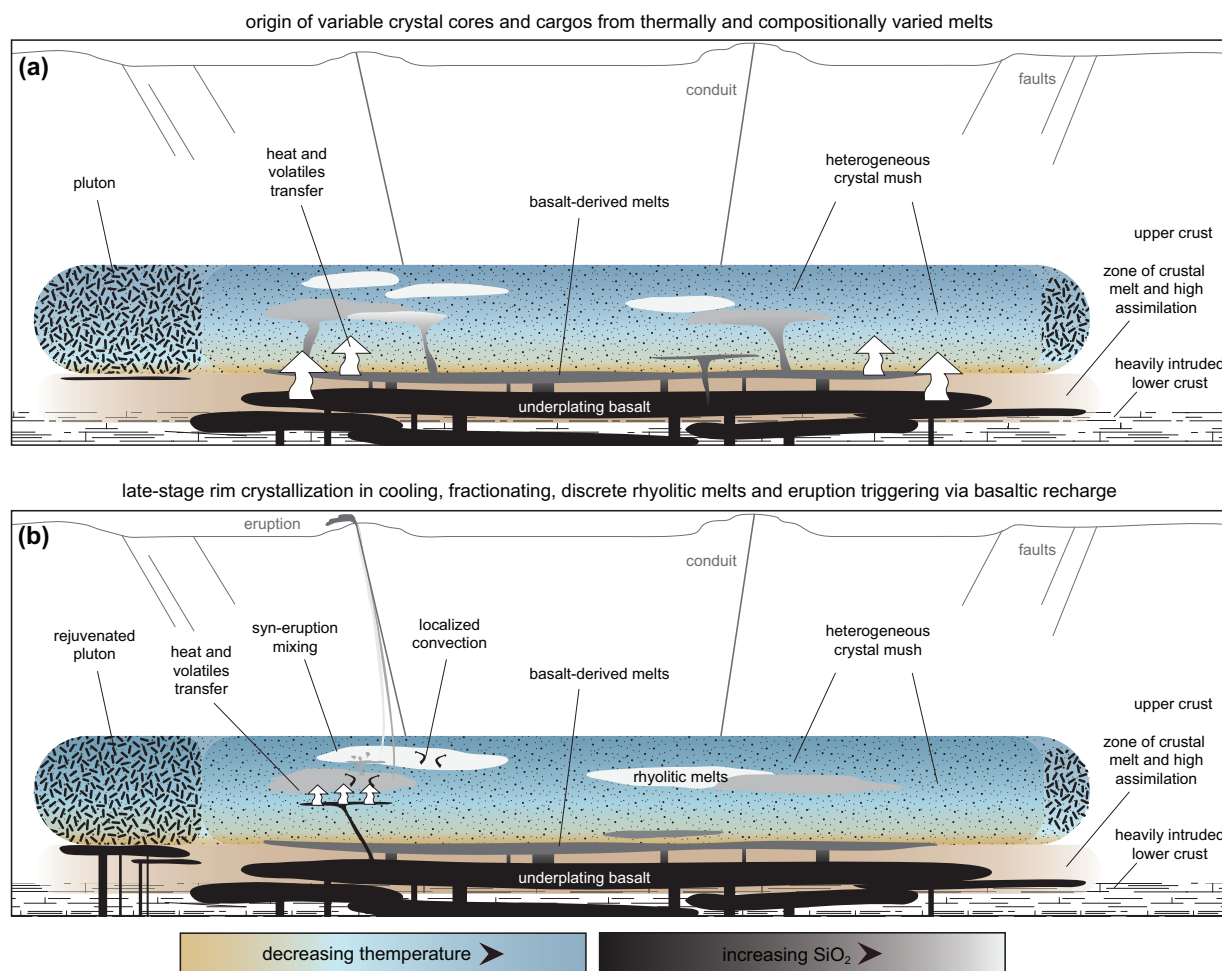
Fig. 11. Sr–Nd isotope results of AFC models (black lines) and mixing models (gray lines) using offshore TVZ basalts as parents and TVZ regional metasediments as assimilants. Potential parental melts are shown as upside-down filled triangles, crustal assimilants and contaminants are shown as filled hexagons, and OVC whole-rock rhyolites (previously published data, Supplementary Data Table A6) are shown as filled orange circles. Symbols on both AFC and mixing lines indicate 10 % increments. (a) Models using a DMM parental source (Ngatoro Basin). (b) Models using a DMM + subduction flux parental source (Rumble IV). All modelling inputs and representative compositions are listed in Table 3. Shaded regions are based on previously published isotopic ratios (Supplementary Data Table A6, references therein).
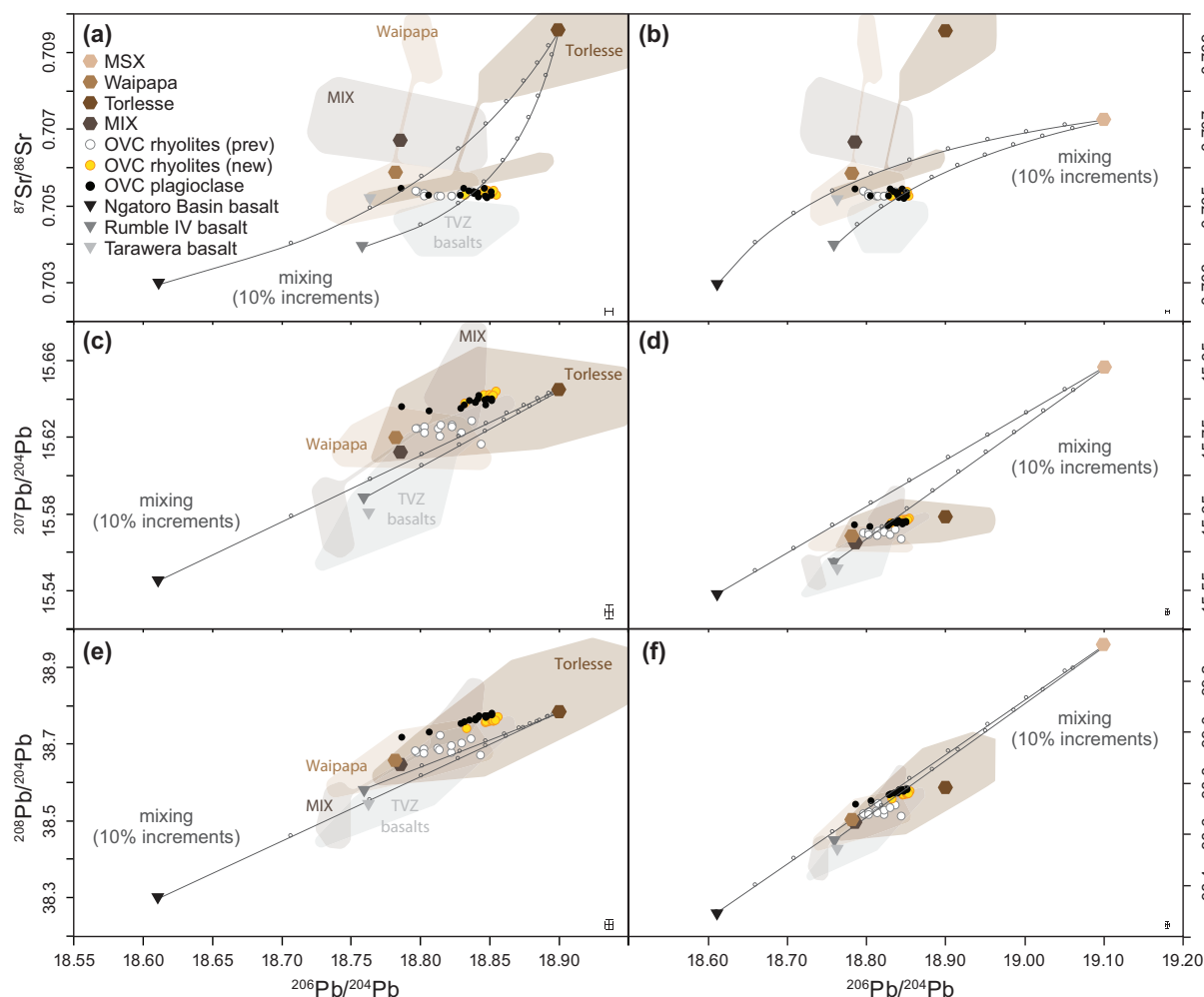
Fig. 12. Sr–Pb isotope mixing (gray lines) models results using offshore TVZ basalts as parents and TVZ regional metasediments as assimilants. Potential parental melts are shown as upside-down filled triangles, crustal assimilants and contaminants are shown as filled hexagons, OVC plagioclase is shown as filled black circles, OVC whole-rock rhyolites are shown as filled orange circles (this study) and white circles (previously published). Error bars represent external error on plagioclase analyses (Supplementary Data Table A3). Steps on the mixing lines indicate 10 % increments. All modelling inputs and representative compositions are listed in Table 3. Shaded regions are based on previously published isotopic ratios (Supplementary Data Table A6; references therein).

origin of variable crystal cores and cargos from thermally and compositionally varied melts

late-stage rim crystallization in cooling, fractionating, discrete rhyolitic melts and eruption triggering via basaltic recharge

Fig. 13. Schematic model of rhyolite petrogenesis at OVC. (a) Generation of multiple melt compositions at OVC that account for compositional variability of crystal cargos in deposits. (b) Mafic influx (potentially driven via seismic activity) triggering eruption, where varied rhyolitic melts ascend rapidly and mingle during eruption. Melt accumulation in (b) would be volumetrically greater for caldera-forming scenarios. The pluton represents the semi-detached source of Earthquake Flat and extra-caldera units, which is largely crystalline (modelled after Molloy *et al.*, 2008).

particularly evident in the rhyodacites and low-SiO_2 rhyolites of the Mangaone Subgroup (45–28 ka; Nairn, 2002; Smith *et al.*, 2002). During this eruptive period following caldera formation, basalt-derived melts infiltrated the OVC silicic reservoir, and the erupted plagioclase crystals record multiple periods of recharge, resorption, and crystallization (Hauparu, 36 ka; Shane, 2015). Following the Mangaone interval (post-23 ka), magmas returned to lower temperature, higher-SiO_2 rhyolites (e.g. Shane & Smith, 2013; Shane, 2015). These younger rhyolites show little evidence of basaltic input based on their plagioclase records (this study). This could reflect regrowth of the crustal magmatic system buffering against direct magma inputs (Shane & Smith, 2013; Shane, 2015).

Basaltic intrusions at OVC also act as an eruption trigger (e.g. Leonard *et al.*, 2002; Shane *et al.*, 2007, 2008*a*; Smith *et al.*, 2010; and others). However, the extent of mass exchange between the intrusive and the high-silica magma is uncertain, and could be fairly limited, as indicated by the pervasive normally zoned

outermost plagioclase rims (Sas *et al.*, 2019; this study). Basaltic clasts, mafic glass shards and discrete tephra beds are associated with some rhyolitic OVC deposits (e.g. Kaharoa, Leonard *et al.*, 2002; Nairn *et al.*, 2004; Okareka, Shane *et al.*, 2008*a*; Rotoiti, Schmitz & Smith, 2004). Nonetheless, the aforementioned studies highlight the small volume of basaltic components in OVC rhyolitic deposits, and also raise the physical limitations that restrict direct rhyolite–basalt mixing (e.g. density, H_2O contents, and viscosity). Hence, we infer that any basalt–rhyolite exchanges are dominated by volatiles and heat (e.g. Shane *et al.*, 2007). Any melt exchange was minor and/or occurred rapidly prior to eruption to maintain the pristine textures (e.g. lack of resorption) and compositions (e.g. normal An zonation) observed in the outermost plagioclase rims. Rapid ascent following eruption triggering has also been previously suggested for Kaharoa plagioclase based on lack of decompression features (Shane, 2015). Rapid ascent is further supported for caldera and intra-caldera units by lack of amphibole

breakdown (Rutherford & Hill, 1993; Shane & Smith, 2013).

A schematic model of the OVC magmatic system is shown in Fig. 13. This model illustrates the complexity of the melt-and-mush OVC magmatic system necessary to reproduce the compositional heterogeneity observed in minerals from a single hand sample. Specifically, it highlights the necessary existence of compositionally discrete melt pockets (Storm *et al.*, 2011) that serve as sources for plagioclase cores. These melts then cool and fractionate to form plagioclase rims. For Earthquake Flat and the extra-caldera domes, the mineral cargos of which probably represent remobilized plutonic fragments, the source is situated on the outer boundary of the main OVC silicic reservoir (after Molloy *et al.*, 2008). The model also demonstrates the important contributions of underplating basalt and crustal assimilation in producing the observed plagioclase intra-crystal and whole-crystal isotopic ratios (Figs 11 and 12).

The model further indicates the importance of extensional processes, despite the OVC being situated in a coupled subduction–extension setting. Specifically, the large proportions ($\geq$20 %) of crustal assimilation are in part possible owing to large volumes of mantle melting and heat flux that are associated with extension-driven decompression (Barker *et al.*, 2020; Zellmer *et al.*, 2020). Additionally, the relative homogeneity of OVC rhyolites and plagioclase (at the resolution of this study) isotopic compositions requires consistent input from both the mantle and crustal sources over the lifespan of the magmatic system (Figs 11 and 12). Such consistency is also largely affected by extension-driven processes and the rapidly thinning crust below the OVC, as it would be difficult to maintain in vertically extensive subduction (e.g. Kimura *et al.*, 2015) or a hotspot (e.g. Hildreth *et al.*, 1991) setting where the crust is notably thicker and inevitably more heterogeneous.

CONCLUSIONS

Large- and small-volume rhyolitic OVC compositions share similar, systematic origins that include extraction of minerals from discrete melts and final growth in fractionating melts. Conclusions are as follows.

1. Disequilibrium textures, variable trace element contents, high and variable Ca/Na ratios, and melts modelled from plagioclase compositions all demonstrate that plagioclase cores are antecrystic and require an initial assembly from compositionally varied melt lenses within a large mush body. Furthermore, the most calcic plagioclase cores indicate nucleation in more mafic melts than OVC rhyolites. However, those melts are not as mafic as OVC basalts, and instead suggest more intermediate origins. Plagioclase isotopic compositions support notable ($\geq$20 %) crustal contamination (calcic cores with

radiogenic $^{87}Sr/^{86}Sr$ and enriched whole-crystal plagioclase Pb isotope ratios).

2. Equilibrium textures, uniform trace element patterns, low Ca/Na ratios, and low-Sr modelled equilibrium melts of plagioclase rims indicate late-stage crystallization in cooling, fractionating, more uniform melts. For caldera and intra-caldera units, those uniform melts are compositionally similar to melt inclusion and whole-rock compositions of the respective unit.

3. Normally zoned, sodic outermost plagioclase rims with no obvious basaltic isotopic signatures suggest that mass exchange between rhyolitic melts and eruption-triggering basaltic melts is limited, and that contributions from the intruding magmas are largely restricted to heat and volatile transfer.

4. Plagioclase and whole-rock Sr–Pb isotopic ratios indicate notable ($\geq$20 %) crustal assimilation of Torlesse-like metasediments with Pb isotopic ratios similar to those of metasedimentary xenoliths. Non-caldera eruptions at the OVC can be modelled using the assimilation of these metasedimentary xenoliths by a subduction-modified DMM parental melt (basalt). However, caldera-forming eruptions require a DMM source with little to no subduction flux (i.e. less radiogenic $^{206}Pb/^{204}Pb$) and greater amounts ($\geq$30 %) of assimilation, suggesting that caldera-forming rhyolitic eruptions in the northern TVZ probably result from large-volume mantle decompression melting events.

5. Similar isotopic compositional ranges of plagioclase crystals imply that relative contributions from isotopically varied sources (i.e. mantle and crust) have largely been consistent across the lifespan of the OVC magmatic system. This differentiates the OVC from other caldera systems worldwide where mass fluctuations have been noted between eruption periods. This difference can probably be attributed to extension-driven processes that provide high mantle melt and heat flux along with a significantly thinned crust beneath the OVC.

The interaction and presence of multiple melts can be explained via a model of disconnected melt pockets within a crystal mush, with remobilization owing to buoyancy-driven gravitational instabilities and heat flux from basalt that underlies the silicic reservoir.

SUPPLEMENTARY DATA

Supplementary data are available at *Journal of Petrology* online.

REFERENCES

Bachmann, O. & Bergantz, G. W. (2008). The magma reservoirs that feed supereruptions. *Elements* **4**, 17–21.

Bannister, S., Bryan, C. J. & Bibby, H. M. (2004). Shear wave velocity variation across the Taupo Volcanic Zone, New Zealand, from receiver function inversion. *Geophysical Journal International* **159**, 291–310.

Barker, S. J., Rowe, M. C., Wilson, C. J. N., Gamble, J. A., Rooyakkers, S. M., Wysoczanski, R. J., Illsley-Kemp, F. & Kenworthy, C. C. (2020). What lies beneath? Reconstructing the primitive magmas fueling voluminous silicic volcanism using olivine-hosted melt inclusions. *Geology* **48**, 504–508.

Blundy, J. & Cashman, K. (2001). Ascent-driven crystallisation of dacite magmas at Mount St Helens, 1980–1986. *Contributions to Mineralogy and Petrology* **140**, 631–650.

Blundy, J. D. & Wood, B. J. (1991). Crystal-chemical controls on the partitioning of Sr and Ba between plagioclase feldspar, silicate melts, and hydrothermal solutions. *Geochimica et Cosmochimica Acta* **55**, 193–209.

Burns, D. H., de Silva, S. L., Tepley, F., Schmitt, A. K. & Loewen, M. W. (2015). Recording the transition from flare-up to steady-state arc magmatism at the Purico–Chascon volcanic complex, northern Chile. *Earth and Planetary Science Letters* **422**, 75–86.

Chadwick, J. P., Troll, V. R., Ginibre, C., Morgan, D., Gertisser, R., Waight, T. E. & Davidson, J. P. (2007). Carbonate assimilation at Merapi Volcano, Java, Indonesia: insights from crystal isotope stratigraphy. *Journal of Petrology* **48**, 1793–1812.

Charlier, B. L. A. & Wilson, C. J. N. (2010). Chronology and evolution of caldera-forming and post-caldera magma systems at Okataina Volcano, New Zealand from zircon U–Th model-age spectra. *Journal of Petrology* **51**, 1121–1141.

Charlier, B. L. A., Peate, D. W., Wilson, C. J. N., Lowenstern, J. B., Storey, M. & Brown, S. J. A. (2003). Crystallisation ages in coeval silicic magma bodies: ^{238}U–^{230}Th disequilibrium evidence from the Rotoiti and Earthquake Flat eruption deposits, Taupo Volcanic Zone, New Zealand. *Earth and Planetary Science Letters* **206**, 441–457.

Charlier, B. L. A., Wilson, C. J. N., Lowenstern, J. B., Blake, S., Van Calsteren, P. W. & Davidson, J. P. (2005). Magma generation at a large, hyperactive silicic volcano (Taupo, New Zealand) revealed by U–Th and U–Pb systematics in zircons. *Journal of Petrology* **46**, 3–32.

Charlier, B. L. A., Bachmann, O., Davidson, J. P., Dungan, M. A. & Morgan, D. J. (2007). The upper crustal evolution of a large silicic magma body: evidence from crystal-scale Rb–Sr isotopic heterogeneities in the Fish Canyon magmatic system. *Journal of Petrology* **48**, 1875–1894.

Charlier, B. L. A., Wilson, C. J. N. & Davidson, J. P. (2008). Rapid open-system assembly of a large silicic magma body: time-resolved evidence from cored plagioclase crystals in the Oruanui eruption deposits, New Zealand. *Contributions to Mineralogy and Petrology* **156**, 799–813.

Cole, J. W., Spinks, K. D., Deering, C. D., Nairn, I. A. & Leonard, G. S. (2010). Volcanic and structural evolution of the Okataina Volcanic Centre; dominantly silicic volcanism associated with the Taupo Rift, New Zealand. *Journal of Volcanology and Geothermal Research* **190**, 123–135.

Cole, J. W., Deering, C. D., Burt, R. M., Sewell, S., Shane, P. A. R. & Matthews, N. E. (2014). Okataina Volcanic Centre, Taupo Volcanic Zone, New Zealand: a review of volcanism and synchronous pluton development in an active, dominantly silicic caldera system. *Earth-Science Reviews* **128**, 1–17.

Costa, F., Chakraborty, S. & Dohmen, R. (2003). Diffusion coupling between trace and major elements and a model for calculation of magma residence times using plagioclase. *Geochimica et Cosmochimica Acta* **67**, 2189–2200.

Couch, S., Sparks, R. S. J. & Carroll, M. R. (2001). Mineral disequilibrium in lavas explained by convective self-mixing in open magma chambers. *Nature* **411**, 1037–1039.

Danišík, M., Shane, P., Schmitt, A. K., Hogg, A., Santos, G. M., Storm, S., Evans, N. J., Keith Fifield, L. & Lindsay, J. M. (2012). Re-anchoring the late Pleistocene tephrochronology of New Zealand based on concordant radiocarbon ages and combined $^{238}U/^{230}Th$ disequilibrium and (U–Th)/He zircon ages. *Earth and Planetary Science Letters* **349–350**, 240–250.

Davidson, J. P., Morgan, D. J., Charlier, B. L. A., Harlou, R. & Hora, J. M. (2007). Microsampling and isotopic analysis of igneous rocks: implications for the study of magmatic systems. *Annual Review of Earth and Planetary Sciences* **35**, 273–311.

Davis, W. J. (1985). Geochemistry and petrology of the Rotoiti and Earthquake Flat pyroclastic deposits. M.S. thesis, Auckland, University of Auckland.

Deering, C. D., Cole, J. W. & Vogel, T. A. (2008). A Rhyolite Compositional Continuum Governed by Lower Crustal Source Conditions in the Taupo Volcanic Zone, New Zealand. *Journal of Petrology* **49**, 2245–2276.

Deering, C. D., Gravley, D. M., Vogel, T. A., Cole, J. W. & Leonard, G. S. (2010). Origins of cold-wet-oxidizing to hot-dry-reducing rhyolite magma cycles and distribution in the Taupo Volcanic Zone, New Zealand. *Contributions to Mineralogy and Petrology* **160**, 609–629.

Dohmen, R. & Blundy, J. (2014). A predictive thermodynamic model for element partitioning between plagioclase and melt as a function of pressure, temperature and composition. *American Journal of Science* **314**, 1319–1372.

Dunstan, L. P., Gramlich, J. W., Barnes, I. L. & Purdy, W. C. (1980). Absolute isotopic abundance and the atomic weight of a reference sample of thallium. *Journal of Research of the National Bureau of Standards* **85**, 1.

Ernst, W. G. & Liu, J. (1998). Experimental phase-equilibrium study of Al- and Ti-contents of calcic amphibole in MORB; a semiquantitative thermobarometer. *American Mineralogist* **83**, 952–969.

Froggatt, P. C. & Lowe, D. J. (1990). A review of late Quaternary silicic and some other tephra formations from New Zealand: their stratigraphy, nomenclature, distribution, volume, and age. *New Zealand Journal of Geology and Geophysics* **33**, 89–109.

Gamble, J. A., Smith, I. E. M., McCulloch, M. T., Graham, I. J. & Kokelaar, B. P. (1993). The geochemistry and petrogenesis of basalts from the Taupo Volcanic Zone and Kermadec Island Arc, SW Pacific. *Journal of Volcanology and Geothermal Research* **54**, 265–290.

Gamble, J. A., Wright, I. C., Woodhead, J. D. & McCulloch, M. T. (1994). Arc and back-arc geochemistry in the southern Kermadec arc—Ngatoro Basin and offshore Taupo Volcanic Zone, SW Pacific. In: Smellie, J. L., Volcanism Associated

with Extension at Consuming Plate Margins *Geological Society, London, Special Publications* **81**, 193–212.

Gamble, J., Woodhead, J., Wright, I. & Smith, I. (1996). Basalt and sediment geochemistry and magma petrogenesis in a transect from oceanic island arc to rifted continental margin arc: the Kermadec–Hikurangi Margin, SW Pacific. *Journal of Petrology* **37**, 1523–1546.

Ghiorso, M. S. & Sack, O. (1991). Fe-Ti oxide geothermometry: thermodynamic formulation and the estimation of intensive variables in silicic magmas. *Contributions to Mineralogy and Petrology* **108**, 485–510.

Ginibre, C. & Davidson, J. P. (2014). Sr isotope zoning in plagioclase from Parinacota Volcano (Northern Chile). *Journal of Petrology* **55**, 1203–1238.

Ginibre, C., Wörner, G. & Kronz, A. (2002). Minor- and trace-element zoning in plagioclase: implications for magma chamber processes at Parinacota volcano, northern Chile. *Contributions to Mineralogy and Petrology* **143**, 300–315.

Ginibre, C., Wörner, G. & Kronz, A. (2007). Crystal zoning as an archive for magma evolution. *Elements* **3**, 261–266.

Graham, I. J., Blattner, P. & McCulloch, M. T. (1990). Meta-igneous granulite xenoliths from Mount Ruapehu, New Zealand: Fragments of altered oceanic crust? *Contributions to Mineralogy and Petrology* **105**, 650–661.

Graham, I. J., Gulson, B. L., Hedenquist, J. W. & Mizon, K. (1992). Petrogenesis of Late Cenozoic volcanic rocks from the Taupo Volcanic Zone, New Zealand, in the light of new lead isotope data. *Geochimica et Cosmochimica Acta* **56**, 2797–2819.

Graham, I. J., Cole, J. W., Briggs, R. M., Gamble, J. A. & Smith, I. E. M. (1995). Petrology and petrogenesis of volcanic rocks from the Taupo Volcanic Zone: a review. *Journal of Volcanology and Geothermal Research* **68**, 59–87.

Harrison, A. & White, R. S. (2006). Lithospheric structure of an active backarc basin: the Taupo Volcanic Zone, New Zealand. *Geophysical Journal International* **167**, 968–990.

Heise, W., Caldwell, T. G., Bibby, H. M. & Bennie, S. L. (2010). Three-dimensional electrical resistivity image of magma beneath an active continental rift, Taupo Volcanic Zone, New Zealand. *Geophysical Research Letters* **37**, L10301.

Hiess, J., Cole, J. W. & Spinks, K. D. (2007). Influence of the crust and crustal structure on the location and composition of high-alumina basalts of the Taupo Volcanic Zone, New Zealand. *New Zealand Journal of Geology and Geophysics* **50**, 327–342.

Hildreth, W., Christiansen, R. L. & O'Neil, J. R. (1984). Catastrophic isotopic modification of rhyolitic magma at times of caldera subsidence, Yellowstone Plateau Volcanic Field. *Journal of Geophysical Research* **89**, 8339–8369.

Hildreth, W., Halliday, A. N. & Christiansen, R. L. (1991). Isotopic and chemical evidence concerning the genesis and contamination of basaltic and rhyolitic magma beneath the Yellowstone Plateau volcanic field. *Journal of Petrology* **32**, 63–138.

Hogg, A. G., Higham, T. F. G., Lowe, D. J., Palmer, J. G., Reimer, P. J. & Newnham, R. M. (2003). A wiggle-match date for Polynesian settlement of New Zealand. *Antiquity* **77**, 116–125.

Houghton, B. F., Wilson, C. J. N., McWilliams, M. O., Lanphere, M. A., Weaver, S. D., Briggs, R. M. & Pringle, M. S. (1995). Chronology and dynamics of a large silicic magmatic system: central Taupo Volcanic Zone, New Zealand. *Geology* **23**, 13–16.

Huang, Y., Hawkesworth, C. J., van Calsteren, P., Smith, I. & Black, P. (1997). Melt generation models for the Auckland volcanic field, New Zealand. *Earth and Planetary Science Letters* **149**, 67–84.

Huang, Y., Hawkesworth, C., Smith, I., van Calsteren, P. & Black, P. (2000). Geochemistry of late Cenozoic basaltic volcanism in Northland and Coromandel, New Zealand: implications for mantle enrichment processes. *Chemical Geology* **164**, 219–238.

Humphreys, M. C. S. (2011). Silicate liquid immiscibility within the crystal mush: evidence from Ti in plagioclase from the Skaergaard intrusion. *Journal of Petrology* **52**, 147–174.

Imai, N., Terashima, S., Itoh, S. & Ando, A. (1995). 1994 compilation values for GSJ reference samples, "Igneous rock series". *Geochemical Journal* **29**, 91–95.

Johnson, E. R., Kamenetsky, V. S., McPhie, J. & Wallace, P. J. (2011). Degassing of the H_2O-rich rhyolites of the Okataina Volcanic Center, Taupo Volcanic Zone, New Zealand. *Geology* **39**, 311–314.

Johnson, E. R., Kamenetsky, V. S. & McPhie, J. (2013). The behavior of metals (Pb, Zn, As, Mo, Cu) during crystallization and degassing of rhyolites from the Okataina Volcanic Center, Taupo Volcanic Zone, New Zealand. *Journal of Petrology* **54**, 1641–1659.

Kimura, J.-I., Nagahashi, Y., Satoguchi, Y. & Chang, Q. (2015). Origins of felsic magmas in Japanese subduction zone: Geochemical characterizations of tephra from caldera-forming eruptions <5 Ma: Origin of caldera eruptions in Japan. *Geochemistry, Geophysics, Geosystems* **16**, 2147–2174.

Klemetti, E. W., Deering, C. D., Cooper, K. M. & Roeske, S. M. (2011). Magmatic perturbations in the Okataina Volcanic Complex, New Zealand at thousand-year timescales recorded in single zircon crystals. *Earth and Planetary Science Letters* **305**, 185–194.

Kobayashi, T., Nairn, I., Smith, V. & Shane, P. (2005). Proximal stratigraphy and event sequence of the *c.* 5600 cal. yr BP Whakatane rhyolite eruption episode from Haroharo volcano, Okataina Volcanic Centre, New Zealand. *Journal of Geology and Geophysics* **48**, 471–490.

Kuritani, T. & Nakamura, E. (2002). Precise isotope analysis of nanogram-level Pb for natural rock samples without use of double spikes. *Chemical Geology* **186**, 31–43.

Kuritani, T. & Nakamura, E. (2003). Highly precise and accurate isotopic analysis of small amounts of Pb using ^{205}Pb–^{204}Pb and ^{207}Pb–^{204}Pb, two double spikes. *Journal of Analytical Atomic Spectrometry* **18**, 1464–1470.

Kuritani, T., Usui, T., Yokoyama, T. & Nakamura, E. (2006). Accurate isotopic and concentration analyses of small amounts of Pb using isotope dilution coupled with the double spike technique. *Geostandards and Geoanalytical Research* **30**, 209–220.

Lange, R. A., Frey, H. M. & Hector, J. (2009). A thermodynamic model for the plagioclase–liquid hygrometer/thermometer. *American Mineralogist* **94**, 494–506.

Leonard, G. S., Begg, J. G. & Wilson, C. J. N. (2010). Geology of the Rotorua Area. Institute of Geological and Nuclear Sciences 1:250,000, geological map 5. 1 sheet + 102 p. Lower Hutt, New Zealand: Institute of Geological and Nuclear Sciences.

Leonard, G. S., Cole, J. W., Nairn, I. A. & Self, S. (2002). Basalt triggering of the *c.* AD 1305 Kaharoa rhyolite eruption, Tarawera volcanic complex, New Zealand. *Journal of Volcanology and Geothermal Research* **115**, 461–486.

Lowe, D. J., Shane, P. A. R., Alloway, B. V. & Newnham, R. M. (2008). Fingerprints and age models for widespread New Zealand tephra marker beds erupted since 30,000 years ago: a framework for NZ-INTIMATE. *Quaternary Science Reviews* **27**, 95–126.

Macpherson, C. G., Gamble, J. A. & Mattey, D. P. (1998). Oxygen isotope geochemistry of lavas from an oceanic to

continental arc transition, Kermadec–Hikurangi margin. *Earth and Planetary Science Letters* **160**, 609–621.

Makishima, A. & Masuda, A. (1994). Ce isotope ratios of N-type MORB. *Chemical Geology* **118**, 1–8.

Martel, C., Radadi Ali, A., Poussineau, S., Gourgaud, A. & Pichavant, M. (2006). Basalt-inherited microlites in silicic magmas: evidence from Mount Pelée (Martinique, French West Indies). *Geology* **34**, 905.

McCulloch, M. T., Kyser, T. K., Woodhead, J. D. & Kinsley, L. (1994). Pb–Sr–Nd–O isotopic constraints on the origin of rhyolites from the Taupo Volcanic Zone of New Zealand: evidence for assimilation followed by fractionation from basalt. *Contributions to Mineralogy and Petrology* **115**, 303–312.

Miller, J. A. & Kent, A. J. R. (2009). The determination of maternal run time in juvenile Chinook salmon (*Oncorhynchus tshawytscha*) based on Sr/Ca and $^{87}Sr/^{86}Sr$ within otolith cores. *Fisheries Research* **95**, 373–378.

Miyazaki, T. & Shuto, K. (1998). Sr and Nd isotope ratios of twelve GSJ rock reference samples. *Geochemical Journal* **32**, 345–350.

Molloy, C., Shane, P. & Nairn, I. (2008). Pre-eruption thermal rejuvenation and stirring of a partly crystalline rhyolite pluton revealed by the Earthquake Flat Pyroclastics deposits, New Zealand. *Journal of the Geological Society, London* **165**, 435–447.

Molloy, C., Shane, P. A. R. & Augustinus, P. (2009). Eruption recurrence rates in a basaltic volcanic field based on tephra layers in maar sediments: Implications for hazards in the Auckland volcanic field. *Geological Society of America Bulletin* **121**, 1666–1677.

Nairn, I. A. (2002). *Geology of the Okataina Volcanic Centre*. Lower Hutt: Institute of Geological and Nuclear Sciences.

Nairn, I. A., Shane, P. R., Cole, J. W., Leonard, G. J., Self, S. & Pearson, N. (2004). Rhyolite magma processes of the ∼AD 1315 Kaharoa eruption episode, Tarawera Volcano, New Zealand. *Journal of Volcanology and Geothermal Research* **131**, 265–294.

Nash, B., Perkins, M., Christensen, J., Lee, D. & Halliday, A. (2006). The Yellowstone hotspot in space and time: Nd and Hf isotopes in silicic magmas. *Earth and Planetary Science Letters* **247**, 143–156.

Nelson, S. T. & Montana, A. (1992). Sieve-textured plagioclase in volcanic rocks produced by rapid decompression. *American Mineralogist* **77**, 1242–1249.

Patiño Douce, A. E. (1993). Titanium substitution in biotite: an empirical model with applications to thermometry, O_2 and H_2O barometries, and consequences for biotite stability. *Chemical Geology* **108**, 133–162.

Pin, C., Briot, D., Bassin, C. & Poitrasson, F. (1994). Concomitant separation of strontium and samarium–neodymium for isotopic analysis in silicate samples, based on specific extraction chromatography. *Analytica Chimica Acta* **298**, 209–217.

Price, R. C., Gamble, J. A., Smith, I. E. M., Stewart, R. B., Eggins, S. & Wright, I. C. (2005). An integrated model for the temporal evolution of andesites and rhyolites and crustal development in New Zealand's North Island. *Journal of Volcanology and Geothermal Research* **140**, 1–24.

Price, R. C., Gamble, J. A., Smith, I. E. M., Maas, R., Waight, T., Stewart, R. B. & Woodhead, J. (2012). The anatomy of an andesite volcano: a time–stratigraphic study of andesite petrogenesis and crustal evolution at Ruapehu Volcano, New Zealand. *Journal of Petrology* **53**, 2139–2189.

Price, R., Mortimer, N., Smith, I. & Maas, R. (2015). Whole-rock geochemical reference data for Torlesse and Waipapa terranes, North Island, New Zealand. *Journal of Geology and Geophysics* **58**, 213–228.

Raczek, I., Stoll, B., Hofmann, A. W. & Jochum, K. P. (2001). High-precision trace element data for the USGS reference materials BCR-1, BCR-2, BHVO-1, BHVO-2, AGV-1, AGV-2, DTS-1, DTS-2, GSP-1 and GSP-2 by ID-TIMS and MIC-SSMS. *Geostandards and Geoanalytical Research* **25**, 77–86.

Raczek, I., Jochum, K. P. & Hofmann, A. W. (2003). Neodymium and strontium isotope data for USGS Reference Materials BCR-1, BCR-2, BHVO-1, BHVO-2, AGV-1, AGV-2, GSP-1, GSP-2 and eight MPI-DING reference glasses. *Geostandards and Geoanalytical Research* **27**, 173–179.

Ramos, F. C. & Tepley, F. J. (2008). Inter- and intracrystalline isotopic disequilibria: techniques and applications. In: Putirka, K. D. and Tepley III, F. J. Minerals, Inclusions And Volcanic Processes. Vol 69, *Mineralogical Society of America and Geochemical Society, Reviews in Mineralogy and Geochemistry* **69**, 403–443.

Rubin, A. E., Cooper, K. M., Till, C. B., Kent, A. J., Costa, F., Bose, M., Gravley, D., Deering, C. & Cole, J. (2017). Rapid cooling and cold storage in a silicic magma reservoir recorded in individual crystals. *Science* **356**, 1154–1156.

Ruprecht, P. & Wörner, G. (2007). Variable regimes in magma systems documented in plagioclase zoning patterns: El Misti stratovolcano and Andahua monogenetic cones. *Journal of Volcanology and Geothermal Research* **165**, 142–162.

Rutherford, M. J. & Hill, P. M. (1993). Magma ascent rates from amphibole breakdown: an experimental study applied to the 1980–1986 Mount St. Helens eruptions. *Journal of Geophysical Research* **98**, 667–685.

Sahetapy-Engel, S., Self, S., Carey, R. J. & Nairn, I. A. (2014). Deposition and generation of multiple widespread fall units from the c. AD 1314 Kaharoa rhyolitic eruption, Tarawera, New Zealand. *Bulletin of Volcanology* **76**, 836.

Sas, M., Kawasaki, N., Sakamoto, N., Shane, P., Zellmer, G. F., Kent, A. J. R. & Yurimoto, H. (2019). The ion microprobe as a tool for obtaining strontium isotopes in magmatic plagioclase: a case study at Okataina Volcanic Centre, New Zealand. *Chemical Geology* **513**, 153–166.

Schmitz, M. D. & Smith, I. E. M. (2004). The petrology of the Rotoiti eruption sequence, Taupo Volcanic Zone: an example of fractionation and mixing in a rhyolitic system. *Journal of Petrology* **45**, 2045–2066.

Self, S. (2006). The effects and consequences of very large explosive volcanic eruptions. *Philosophical Transactions of the Royal Society of London, Series A* **364**, 2073–2097.

Shane, P. A. R. (1998). Correlation of rhyolitic pyroclastic eruptive units from the Taupo volcanic zone by Fe-Ti oxide compositional data. *Bulletin of Volcanology* **60**, 224–238.

Shane, P. A. R. (2015). Contrasting plagioclase textures and geochemistry in response to magma dynamics in an intra-caldera rhyolite system, Okataina Volcano. *Journal of Volcanology and Geothermal Research* **297**, 1–10.

Shane, P. A. R. & Smith, V. C. (2013). Using amphibole crystals to reconstruct magma storage temperatures and pressures for the post-caldera collapse volcanism at Okataina Volcano. *Lithos* **156–159**, 159–170.

Shane, P. A. R., Nairn, I. A. & Smith, V. C. (2005). Magma mingling in the ∼50 ka Rotoiti eruption from Okataina Volcanic Centre: implications for geochemical diversity and chronology of large volume rhyolites. *Journal of Volcanology and Geothermal Research* **139**, 295–313.

Shane, P. A. R., Martin, S. B., Smith, V. C., Beggs, K. F., Darragh, M. B., Cole, J. W. & Nairn, I. A. (2007). Multiple rhyolite magmas and basalt injection in the 17·7 ka Rerewhakaaitu eruption episode from Tarawera Volcanic Complex, New Zealand. *Journal of Volcanology and Geothermal Research* **164**, 1–26.

Shane, P. A. R., Nairn, I. A., Smith, V. C., Darragh, M., Beggs, K. & Cole, J. W. (2008a). Silicic recharge of multiple rhyolite magmas by basaltic intrusion during the 22·6 ka Okareka Eruption Episode, New Zealand. *Lithos* **103**, 527–549.

Shane, P. A. R., Smith, V. C. & Nairn, I. A. (2008b). Millennial timescale resolution of rhyolite magma recharge at Tarawera Volcano: insights from quartz chemistry and melt inclusions. *Contributions to Mineralogy and Petrology* **156**, 397–411.

Singer, B. S., Dungan, M. A. & Layne, G. D. (1995). Textures and Sr, Ba, Mg, Fe, K, and Ti compositional profiles in volcanic plagioclase: clues to the dynamics of calc-alkaline magma chambers. *American Mineralogist* **80**, 776–798.

Sisson, T. W. & Grove, T. L. (1993). Temperatures and H_2O contents of low-MgO high-alumina basalts. *Contributions to Mineralogy and Petrology* **113**, 167–184.

Smith, V. C., Shane, P. A. R. & Smith, I. E. M. (2002). Tephrostratigraphy and geochemical fingerprinting of the Mangaone subgroup tephra beds, Okataina Volcanic Centre, New Zealand. *New Zealand Journal of Geology and Geophysics* **45**, 207–219.

Smith, V. C., Shane, P. A. R. & Nairn, I. A. (2005). Trends in rhyolite geochemistry, mineralogy, and magma storage during the last 50 kyr at Okataina and Taupo Volcanic Centres, Taupo Volcanic Zone, New Zealand. *Journal of Volcanology and Geothermal Research* **148**, 372–406.

Smith, V. C., Shane, P. A. R., Nairn, I. A. & Williams, C. M. (2006). Geochemistry and magmatic properties of eruption episodes from Haroharo linear vent zone, Okataina Volcanic Centre, New Zealand during the last 10 kyr. *Bulletin of Volcanology* **69**, 57–88.

Smith, V. C., Shane, P. A. R. & Nairn, I. A. (2010). Insights into silicic melt generation using plagioclase, quartz and melt inclusions from the caldera-forming Rotoiti eruption, Taupo Volcanic Zone, New Zealand. *Contributions to Mineralogy and Petrology* **160**, 951–971.

Spell, T. L., Kyle, P. R., Thirlwall, M. F. & Campbell, A. R. (1993). Isotopic and geochemical constraints on the origin and evolution of postcollapse rhyolites in the Valles Caldera, New Mexico. *Journal of Geophysical Research: Solid Earth* **98**, 19723–19739.

Spinks, K. D., Acocella, V., Cole, J. W. & Bassett, K. N. (2005). Structural control of volcanism and caldera development in the transtensional Taupo Volcanic Zone, New Zealand. *Journal of Volcanology and Geothermal Research* **144**, 7–22.

Stern, T. & Benson, A. (2011). Wide-angle seismic imaging beneath an andesitic arc: Central North Island, New Zealand. *Journal of Geophysical Research* **116**, 1–26.

Storm, S., Shane, P. A. R., Schmitt, A. K. & Lindsay, J. M. (2011). Contrasting punctuated zircon growth in two syn-erupted rhyolite magmas from Tarawera Volcano: Insights to crystal diversity in magmatic systems. *Earth and Planetary Science Letters* **301**, 511–520.

Storm, S., Shane, P. A. R., Schmitt, A. K. & Lindsay, J. M. (2012). Decoupled crystallization and eruption histories of the rhyolite magmatic system at Tarawera Volcano revealed by zircon ages and growth rates. *Contributions to Mineralogy and Petrology* **163**, 505–519.

Storm, S., Schmitt, A. K., Shane, P. A. R. & Lindsay, J. M. (2014). Zircon trace element chemistry at sub-micrometer resolution for Tarawera Volcano, New Zealand, and implications for rhyolite magma evolution. *Contributions to Mineralogy and Petrology* **167**, 1000.

Streck, M. J. (2008). Time scales of magmatic processes from modeling the zoning patterns of crystals. In: Putirka, K. D. and Tepley III, F. J. Minerals, Inclusions And Volcanic Processes. Vol 69. *Mineralogical Society of America and Geochemical Society, Reviews in Mineralogy and Geochemistry* **69**, 595–622.

Taylor, R. N., Ishizuka, O., Michalik, A., Milton, J. A. & Croudace, I. W. (2015). Evaluating the precision of Pb isotope measurement by mass spectrometry. *Journal of Analytical Atomic Spectrometry* **30**, 198–213.

Tepley, F. J., Davidson, J. P. & Clynne, M. A. (1999). Magmatic interactions as recorded in plagioclase phenocrysts of Chaos Crags, Lassen Volcanic Center, California. *Journal of Petrology* **40**, 787–806.

Tepley, F. J., Davidson, J. P., Tilling, R. I. & Arth, J. G. (2000). Magma mixing, recharge and eruption histories recorded in plagioclase phenocrysts from El Chichon Volcano. *Journal of Petrology* **41**, 1397–1411.

Timm, C., Hoernle, K., Werner, R., Hauff, F., van den Bogaard, P., White, J., Mortimer, N. & Garbe-Schönberg, D. (2010). Temporal and geochemical evolution of the Cenozoic intraplate volcanism of Zealandia. *Earth-Science Reviews* **98**, 38–64.

Waight, T. E., Troll, V. R., Gamble, J. A., Price, R. C. & Chadwick, J. P. (2017). Hf isotope evidence for variable slab input and crustal addition in basalts and andesites of the Taupo Volcanic Zone, New Zealand. *Lithos* **284–285**, 222–236.

Wallace, L. M., Beavan, J., McCaffrey, R. & Darby, D. (2004). Subduction zone coupling and tectonic block rotations in the North Island, New Zealand. *Journal of Geophysical Research* **109**, B12406.

Wallace, L. M., Reyners, M., Cochran, U., Bannister, S., Barnes, P. M., Berryman, K., Downes, G., Eberhart-Phillips, D., Fagereng, A., Ellis, S., Nicol, A., McCaffrey, R., Beavan, R. J., Henrys, S., Sutherland, R., Barker, D. H. N., Litchfield, N., Townend, J., Robinson, R., Bell, R., Wilson, K. & Power, W. (2009). Characterizing the seismogenic zone of a major plate boundary subduction thrust: Hikurangi Margin, New Zealand. *Geochemistry, Geophysics, Geosystems* **10**, Q10006.

Wilson, C. J. N. & Charlier, B. L. A. (2016). The life and times of silicic volcanic systems. *Elements* **12**, 103–108.

Wilson, C. J. N., Houghton, B. F., McWilliams, M. O., Landphere, M. A., Weaver, S. D. & Briggs, R. M. (1995). Volcanic and structural evolution of Taupo Volcanic Zone, New Zealand: a review. *Journal of Volcanology and Geothermal Research* **68**, 1–28.

Wolff, J. A. & Ramos, F. C. (2014). Processes in caldera-forming high-silica rhyolite magma: Rb–Sr and Pb isotope systematics of the Otowi Member of the Bandelier Tuff, Valles Caldera, New Mexico, USA. *Journal of Petrology* **55**, 345–375.

Woodhead, J. D., Volker, F. & McCulloch, M. T. (1995). Routine lead isotope determinations using a lead-207–lead-204 double spike: a long-term assessment of analytical precision and accuracy. *Analyst* **120**, 35–39.

Zellmer, G. F., Blake, S., Vance, D., Hawkesworth, C. J. & Turner, S. (1999). Plagioclase residence times at two island arc volcanoes (Kameni Islands, Santorini, and Soufriere, St. Vincent) determined by Sr diffusion systematics. *Contributions to Mineralogy and Petrology* **136**, 345–357.

Zellmer, G. F., Sparks, R. S. J., Hawkesworth, C. J. & Wiedenbeck, M. (2003). Magma emplacement and remobilization timescales beneath Montserrat: insights from Sr and Ba zonation in plagioclase phenocrysts. *Journal of Petrology* **44**, 1413–1431.

Zellmer, G. F., Kimura, J.-I., Stirling, C. H., Lube, G., Shane, P. A. & Iizuka, Y. (2020). Genesis of recent mafic magmatism in the Taupo Volcanic Zone, New Zealand: insights into the birth and death of very large volume rhyolitic systems? *Journal of Petrology* **61**,